



Tailoring MgO-based supported Rh catalysts for purification of gas streams from phenol

K. Polychronopoulou^a, K. Giannakopoulos^{b,c}, A.M. Efstathiou^{a,*}

^a Chemistry Department, Heterogeneous Catalysis Laboratory, University of Cyprus, P.O. Box 20537, 1678 Nicosia, Cyprus

^b Institute of Materials Science, N.C.S.R. "Demokritos", Patriarchou Gregoriou & Neapoleos, 15310 Agia Paraskevi, Athens, Greece

^c Institute of Microelectronics, N.C.S.R. "Demokritos", Patriarchou Gregoriou & Neapoleos, 15310 Agia Paraskevi, Athens, Greece

ARTICLE INFO

Article history:

Received 5 August 2011

Received in revised form 9 October 2011

Accepted 11 October 2011

Available online 18 October 2011

Keywords:

Phenol steam reforming

Supported Rh catalysts

MgO-based solid supports

In situ XRD

X-ray photoelectron spectroscopy

High resolution transmission electron microscopy

H₂-TPR

ABSTRACT

The present work is focused on the sol–gel synthesis, characterization and catalytic performance evaluation of novel Mg–Ce–Zr–O-based mixed oxides supported Rh catalysts for the purification of H₂-rich gas streams from phenol through steam reforming in the 575–730 °C range. Phenol is used as a model compound of tars, the former being one of the main constituents of tars formed during steam gasification and pyrolysis of biomass. Novel Rh catalysts (0.1 wt%) supported on Mg–Ce–Zr–O-based mixed oxides modified by alkaline-earth, rare earth, and transition metal ions, having the general formula Mg–Ce–Zr–X–O (where X stands for La, Sr, Ba, Ca and Zn) were systematically studied. The physicochemical properties of the catalysts were evaluated using complementary bulk and surface characterization techniques, such as BET, XPS, *in situ* XRD, TEM/SAED and SEM/EDX. Transient techniques including H₂-TPR, TPD-CO₂ and TPD-NH₃ were employed in order to characterize redox behavior, surface basicity, and surface acidity of support, respectively. Among the catalysts examined, a 0.1 wt% Rh/40Mg–20Ce–20Zr–20La–O was found to exhibit the highest hydrogen product yield, specific H₂ production rate (μmol/m² min), and the lowest CO/CO₂ product ratio (575–730 °C), even when compared to a Ni-based commercial steam reforming of tars catalyst. At 655 °C, a H₂ yield of ~95% and a specific reaction rate of 100 μmol H₂/m² min were obtained for a feed containing 0.5 vol% phenol and 40 vol% H₂O at a gas hourly space velocity of ~80,000 h^{−1}. This activity behavior is correlated with the largest concentration of basic sites and labile oxygen species (μmol/m²), and also with the largest acid/base site ratio present in the 40Mg–20Ce–20Zr–20La–O support composition. Steam was also found to be an efficient reagent for the removal of carbonaceous deposits (e.g., C_xH_y) formed on the catalyst surface during phenol steam reforming. The H/C atom compositional ratio of the carbonaceous deposits was found to depend on reaction temperature.

© 2011 Elsevier B.V. All rights reserved.

1. Introduction

Hydrogen becomes an important alternative clean fuel that can be used in fuel cells and internal combustion engines for power generation, if produced from renewable sources. Biomass (renewable energy source) can be used as an attractive raw feedstock for H₂ production through possible technologies, namely: steam gasification [1–3] and catalytic steam reforming of pyrolysis oils [4,5]. The advantages of biomass over other feedstock is that by adopting proper use of biomass conversion technologies and good practices, CO₂ emissions can be limited to a good extent [6]. For example, by adopting coppicing in the woodland management, up to 80% reduction in emissions can be achieved if compared to the use of natural gas [7]. Other parameters, such as biomass type, land used, and N-fertilization can have an important impact in getting the most out

of biomass. In terms of carbon balance, it has been reported that in the case of a biomass IGCC plant, because part of CO₂ emitted is recycled (biomass growing), the net emissions can be in the order of 4.5% of those arising from a coal-based IGCC plant [8,9].

Biomass gasification leads to a mixture of gases mainly consisting of CO_x and H₂, and variable amounts of ash solid particles and tars (liquid form). The latter is considered as one of the most critical problems in biomass gasification. Upgrading the value of H₂-containing gas product stream through an appropriate clean-up process seems to be a mandatory task for the ultimate successful commercial production of H₂-rich gas, allowing its exploitation in energy-related technologies, such as fuel cells and higher efficiency power plants [10,11].

"Tars" is considered to be the condensable fraction of the organic gasification product, a complex mixture of aromatic compounds with molecular weight higher than that of benzene [12]. Tarry compounds are formed in a series of complex reactions and their chemical identity is highly dependent on the operational conditions, feed biomass type, feedstock pretreatment, heating rate,

* Corresponding author. Tel.: +357 22 892776; fax: +357 22 892801.

E-mail address: efstath@ucy.ac.cy (A.M. Efstathiou).

residence time, and pressure [12,13]. Among the applied technologies for “tars” destruction, catalytic decomposition is the most promising one and is industrially performed in the 650–900 °C range using mainly supported-Ni catalysts [14]. The latter, although their wide application in “tars” catalytic decomposition, they suffer from severe coke deposition leading to deterioration of their catalytic performance [14].

Coking issues can be effectively tackled using noble metal supported catalysts (Pt, Rh), the high cost of which is compensated by using low metal loadings, ca. 0.1–0.5 wt%, and which result in high specific activities. It has been reported [15] that suppression of carbon formation is accomplished by decreasing the surface acidity of the catalyst. Towards this direction, the addition of basic oxides on the carrier is expected to increase the rate of carbon gasification due to enhancement of water adsorption [15]. There are many studies concerning the addition of alkali, alkaline-earth, and rare earth oxides as additives towards reduction of carbonaceous deposits, particularly in the formulation of industrial Ni catalysts [16]. In addition, the use of supports having increased concentration of basic sites is expected to strengthen the ability of the catalyst to adsorb CO₂, thus suppressing carbon formation through the Boudouart reaction ($2\text{CO(g)} \rightleftharpoons \text{CO}_2\text{(g)} + \text{C(s)}$) [17,18]. Besides the fact that the support composition influences catalyst's coke resistivity, the latter is also related to metal–support interactions, since M–O–M' bond strength is influenced by the M (metal) and M' (support metal cation) chemical nature. It is worthwhile to mention here that small Rh crystallites were found to be less prone to coke deactivation [19].

Many studies have been performed towards the development of catalysts with increased resistivity against coke formation [20–23]. It has been reported that the presence of MgO in the support causes prolongation of induction period during which practically no formation of carbon is obtained [24,25]. For phenol steam reforming, the presence of MgO was shown to lead to enhanced activity over Rh-based catalyst compositions through the boosting of WGS reaction activity, reducibility and OSC of support [26]. On the other hand, La₂O₃ has been used as a promoter due to its beneficiary effect in the steam gasification in the case of pine sawdust [27], steam reforming of bio-oil [15], and steam reforming of naphthalene [28]. La₂O₃ has been also found to stabilize carbonate species on the surface, which potentially act as a source of reactive oxygen, thus facilitating carbon gasification. These catalyst design concepts have been applied in the case of methane steam reforming, where Ni catalysts are widely used. Tsipouriari et al. [29] reported on lanthana-supported Ni catalysts which exhibit enhanced stability towards coking due to the decoration of Ni particles with lanthanum oxy-carbonate species. Also, Matas Güell et al. [30] reported on the improvement in stability of Ni/ZrO₂-based catalysts for steam reforming of acetic acid by the addition of small amounts of K and La. Other studies [31–33] reported on lanthana-modified Pt catalysts towards reduction of support acidity, and prevention of metal sintering. It is also known that chemical modification of support could facilitate partial insertion of the metal to the support, which leads to retardation of metal particles sintering [34,35]. This kind of chemical modification of support opens new possibilities towards the preparation of tailored-made supported catalysts.

Another issue in steam reforming reaction besides coke deposition, as discussed above, is the presence of CO₂ in the reformat gas. In terms of environmental benefits and sustainability, any suggested technology for H₂ production should at least ensure minimum emissions of CO₂ in the atmosphere. One effective way to tackle this problem is by exploiting the absorption enhanced reforming (AER) concept [36]. According to this technology, a natural CO₂-absorbent material (e.g., calcites, dolomites, etc.) or a low-cost synthetic material is mixed with the reforming/gasification catalyst in order to *in situ* remove CO₂ from the

reaction zone and at the same time to shift the water-gas shift reaction towards higher H₂ yields [36]. We have demonstrated the AER concept successfully in the case of phenol steam reforming over supported-Fe catalysts [37].

The main objective of the present work, which is a continuation of our previous works on phenol steam reforming over Rh [38,39] and Fe-based [37] catalysts, is the critical assessment of the effect of support chemical modification in supported Rh catalysts through the addition of alkaline-earth, rare earth metal oxides, and transition metal oxides, on the phenol steam reforming reaction. The latter is considered as an attractive process for the purification of H₂-containing gas streams from phenol in a fixed-bed reactor placed downstream the main reforming/gasification reactor. Fundamental parameters such as: (a) support chemical composition, (b) support surface acidity/basicity and reducibility, (c) reaction temperature, and (d) coke formation are investigated in an effort to gather fundamental information for the correct interpretation of catalytic performance of the former solids.

2. Experimental

2.1. Catalyst preparation

The synthesis procedure of the two series of MgO-based mixed metal oxides, namely 40Mg-25Ce-25Zr-10X-O and 40Mg-20Ce-20Zr-20X-O, where X stands for Sr, La, Ca, Ba and Zn was as follows. Appropriate amounts of magnesium ethoxide (Sigma-Aldrich, 98%) were dissolved in an ethanol/water (6/4, v/v) solvent mixture, while those of cerium nitrate hexahydrate (Sigma-Aldrich, 99%), strontium nitrate (Sigma-Aldrich, >99%), lanthanum nitrate hexahydrate (Sigma-Aldrich, >99%), calcium nitrate tetrahydrate (Sigma-Aldrich, >99%), barium nitrate (Sigma-Aldrich, >99%) or zirconium oxychloride octahydrate (Sigma-Aldrich, >98%) were dissolved in distilled water. For the synthesis of mixed metal oxides, appropriate amounts of each solution were mixed together so as to obtain the desired Mg:Ce:Zr:X atom ratio. The resulting solution was kept at 60 °C for 6 h until viscous yellow-like gels were obtained. After synthesis and drying (overnight at 120 °C), all solids were calcined in air at 750 °C for 4 h, cooled slowly to room temperature, and stored for further use. A reference to a support chemical composition in the rest of the text will be according to the following example. A 40Mg-25Ce-25Zr-10X-O mixed metal oxide will be referred to that having a metal atom % composition of 40Mg, 25Ce, 25Zr and 10X.

The supported Rh catalysts were prepared by the wet impregnation (WI) method using Rh(NO₃)₃ (Aldrich) and distilled de-ionised water. A given amount of precursor solution corresponding to the Rh metal loading of interest was used to impregnate the metal oxide support in powder form at 40 °C. After impregnation and drying (*T* = 120 °C, overnight), the obtained solid was calcined in air at 600 °C for 2 h and stored for further use. Prior to any catalytic tests, the fresh sample (Rh/support) was reduced *in situ* in pure H₂ (1 bar) at 300 °C for 2 h. A commercial nickel-based catalyst (44 wt% NiO/γ-Al₂O₃, Süd-Chemie, code C11-PR) used in “tars” steam reforming was also tested for comparison purposes against the present lab-synthesized 0.1 wt% Rh/Mg-Ce-Zr-X-O catalysts.

2.2. Catalyst characterization

2.2.1. Specific surface area measurements

The specific surface area (SSA, m² g⁻¹) of the fresh supported Rh catalysts, the supports of which were prepared by the sol-gel method (Section 2.1) was checked by N₂ adsorption at 77 K (BET method) using a multipoint Fisons Sorptory 1900 System. Before any

measurements were taken, the samples were outgassed at 300 °C under vacuum ($P \sim 1.3 \times 10^{-3}$ mbar) overnight.

2.2.2. *In situ* XRD studies

The crystal structure of the Mg-Ce-Zr-X-O mixed metal oxides was checked by XRD (Shimadzu 6000 series) after employing CuK α radiation ($\lambda = 1.5418$ Å). For the Rh/Mg-Ce-Zr-X-O catalysts that exhibited best performance towards phenol steam reforming, *in situ* XRD profiles of their supports were recorded in 20 vol% O₂/Ar gas flow in the 300–700 °C range. Following this treatment, XRD profiles were recorded also in 20 vol% H₂/Ar gas flow in the same temperature range. Therefore, the evolution with temperature of solids redox behavior, crystalline phases, and mean primary crystallite size was investigated. The structure evolution of the solid supports under a simulated gas product composition (5% H₂/5% CO/5% CO₂/He) was also investigated, with emphasis in the presence of carbonate phases. The sol–gel synthesized supports after drying at 120 °C were calcined in air only at 300 °C for 4 h before the *in situ* XRD measurements.

2.2.3. SEM/EDX studies

The secondary particle size and surface morphology of some of the supports were examined using a JEOL JSM 5200 scanning electron microscope (25 kV). Powdered specimens were spread on the SEM slabs and sputtered with gold. EDX studies were performed using a PGT detector.

2.2.4. HR-TEM studies

The microstructure and morphology of some of the sol–gel prepared supports were investigated by a Philips CM20 high resolution transmission electron microscope (LaB6 filament) equipped with an energy dispersive X-ray detector. Selected area electron diffraction (SAED) patterns were also recorded.

2.2.5. X-ray photoelectron spectroscopy studies

X-ray photoelectron spectroscopy (XPS) studies were conducted on a VG Escalab 200R spectrometer equipped with a hemispherical electron analyzer and an MgK α (1253.6 eV) X-ray source. The XP spectrometer was maintained at a base pressure of $\sim 8 \times 10^{-10}$ mbar, and it was equipped with a chamber for sample treatment under controlled gas atmosphere (1 atm) and at temperatures lower than 700 °C. A certain region of the XP spectrum was scanned a number of times in order to obtain a good signal to noise ratio. The binding energies (BEs) were referenced to the C 1s peak (285 eV) to account for charging effects. The areas of the peaks were computed by fitting the experimental spectra to Gaussian/Lorentzian curves after removing the background using the Shirley function. Surface atom ratios were calculated from normalised peak area ratios using the corresponding atomic sensitivity factors. The experimental error in surface composition and atom ratios estimation is considered to be less than 10%.

2.2.6. H₂ temperature-programmed reduction studies

Hydrogen temperature-programmed reduction (H₂-TPR) traces were obtained using a 0.2-g solid sample placed in a quartz microreactor, the exit of which was connected to a mass spectrometer (Balzer Prisma QMS 200) for *on line* gas analysis. The gas flow rate was 50 NmL/min (5 vol% H₂/Ar) and the heating rate was 30 °C/min (25–850 °C). The H₂ ($m/z=2$) and H₂O ($m/z=18$) signals in the mass spectrometer were continuously monitored in order to follow the kinetics of reduction of the supported Rh catalysts investigated. Gas lines from the exit of reactor to the inlet of the mass spectrometer were kept at 120 °C in order to avoid water condensation. The H₂-TPR traces obtained were expressed as reduction rate, Rate_{H₂} ($\mu\text{mol H}_2/\text{g min}$) versus temperature, after calibrating

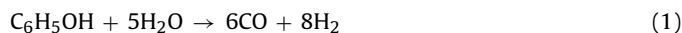
the MS signal with a standard 1 vol% H₂/He gas mixture and using the appropriate material balance.

2.2.7. Temperature-programmed desorption studies

Temperature-programmed desorption (TPD) of NH₃ and CO₂ studies was conducted in order to investigate the surface acidity and basicity, respectively, of the mixed metal oxide supports. The amount of sample used was 0.2 g placed in a quartz microreactor, the exit of which was connected to a mass spectrometer (Balzer Prisma QMS 200) for *on line* gas analysis. The heating rate was 30 °C/min, and the He gas flow rate was 30 NmL/min. The mass numbers (m/z) 15, 30 and 44 were used for NH₃, NO and N₂O (NH₃-TPDs), while the (m/z) 28 and 44 were used for CO and CO₂, respectively in the CO₂-TPDs. NH₃ or CO₂ chemisorption was conducted at 25 °C for 30 min using 2 vol% NH₃/He or 5 vol% CO₂/He gas mixture, respectively. After calibrating the MS signal with standard 1% NH₃/He and 1% CO₂/He gas mixtures, and using the appropriate material balance, the NH₃ and CO₂ uptakes ($\mu\text{mol/g}$) were estimated.

2.3. Catalytic performance studies

The experimental apparatus used for evaluating the catalytic performance of supported Rh solids for the phenol steam reforming has been described in detail elsewhere [39]. A 0.3-g catalyst sample in powder form ($d_p = 0.1$ – 0.2 mm) was loaded into the microreactor. The total gas flow rate used was 200 NmL/min, providing a GHSV of $\sim 80,000$ h^{−1}. The following reaction scheme can be considered to describe the steam reforming of phenol reaction [38–41]:



The hydrogen yield, $Y_{\text{H}_2}(\%)$, and phenol conversion, $X_p(\%)$, were estimated based on the following relationships:

$$Y_{\text{H}_2}(\%) = \frac{y_{\text{H}_2}^{\text{exp}}}{y_{\text{H}_2}^{\text{th}}} \times 100 \quad (3)$$

$$y_{\text{H}_2}^{\text{th}} = \frac{8}{6}y_{\text{CO}} + \frac{14}{6}y_{\text{CO}_2} \quad (4)$$

$$X_p(\%) = \left[\frac{F_{\text{CO}} + F_{\text{CO}_2}}{6F_p^{\text{in}}} \right] \times 100 \quad (5)$$

In Eqs. (3)–(5), $y_{\text{H}_2}^{\text{exp}}$ is the measured mole fraction of hydrogen at the exit gas stream of reactor, $y_{\text{H}_2}^{\text{th}}$ is the theoretical mole fraction of H₂ expected by the network of reactions (1) and (2) and after considering 100% phenol conversion, and y_i , F_i , are the mole fraction and molar flow rate (mol/s), respectively, of component i in the exit gas product stream of reactor. In Eq. (4), the coefficients 8/6 and 14/6 represent the correspondence of 1 mol of H₂ to that of CO and CO₂ formed, respectively, based on the network of reactions (1) and (2). Also, it is noted that only very small concentrations of benzene and methane were measured in the product gas stream, and these are not included in Eq. (5). The carbon mass balance was checked in several experimental runs and it was found to be within 10%. However, it was not possible to perform a reliable hydrogen mass balance due to the high H₂O content used in the feed, and the fact that water was removed by condensation before analysis of the reactor gas effluent stream [39].

2.4. Characterization of carbonaceous deposits by transient experiments

The amount and reactivity towards oxygen and steam of carbon-containing intermediate species formed on the surface of 0.1 wt%

Table 1SSA ($\text{m}^2 \text{g}^{-1}$) of the fresh^a 0.1 wt% Rh/Mg-Ce-Zr-X-O catalysts (X = La, Zn, Ca, Ba, Sr).

Support chemical composition	SSA ($\text{m}^2 \text{g}^{-1}$)
50Mg-25Ce-25Zr-O	30.5
40Mg-25Ce-25Zr-10La-O	21.9
40Mg-25Ce-25Zr-10Zn-O	15.8
40Mg-25Ce-25Zr-10Ca-O	23.0
40Mg-25Ce-25Zr-10Ba-O	18.3
40Mg-25Ce-25Zr-10Sr-O	21.5
40Mg-20Ce-20Zr-20La-O	13.3
40Mg-20Ce-20Zr-20Ba-O	17.9
40Mg-25Ce-25Zr-20Zn-O	15.8
40Mg-25Ce-25Zr-20Sr-O	11.6
40Mg-25Ce-25Zr-20Ca-O	12.5

^a After synthesis of support material (Section 2.1), the supported Rh catalyst was further calcined in air at 600 °C.

Rh/40Mg-20Ce-20Zr-20La-O catalyst after phenol steam reforming were studied by two different transient experiments. In the first experiment, following reaction (0.5% $\text{C}_6\text{H}_5\text{OH}/40\% \text{H}_2\text{O}/\text{He}$) at 655 °C for 3 h, the catalyst was heated to 800 °C in He flow to remove adsorbed water, CO_2 and/or carbonaceous deposits that could thermally be decomposed in He flow. The reactor was then cooled quickly in He flow to room temperature, and the gas flow was switched to a 20 vol% O_2/He gas mixture for a temperature-programmed oxidation (TPO) experiment ($\beta = 30^\circ \text{C}/\text{min}$). In the second transient experiment, after reaction at 655 °C or 755 °C for 3 h, the feed was changed to He until the H_2 , CO, and CO_2 mass spectrometer signals reached practically their respective baseline value. The feed was then switched to a 40% $\text{H}_2\text{O}/2\% \text{Ar}/\text{He}$ gas mixture, and the H_2 ($m/z = 2$), CO ($m/z = 28$), and CO_2 ($m/z = 44$) MS signals were recorded continuously. Quantification of the CO and CO_2 signals was made after accounting for the contribution of CO_2 to the 28 (m/z) signal and using standard calibration gas mixtures in He diluent gas for the CO and CO_2 . Transient experiments were conducted in a specially designed gas flow-system that was described elsewhere [42].

3. Results and discussion

3.1. Catalyst characterization

3.1.1. Surface area and crystal structure

The specific surface area ($\text{m}^2 \text{g}^{-1}$) of all the supports prepared is listed in Table 1. It is observed that the SSA is in the 11–30 $\text{m}^2 \text{g}^{-1}$ range. The SSA of the reference support (50Mg-25Ce-25Zr-O) was reported to be 30.5 $\text{m}^2 \text{g}^{-1}$ [38], whereas after the addition of alkaline-earth (Ca, Sr, Ba), rare earth (La) and transition metal (Zn) ions, the SSA values measured decreased in all cases (Table 1). Rohart et al. [43] noticed an increase of SSA in a Ce-Zr-O solid when La_2O_3 , Pr_6O_{11} or Nd_2O_3 was added. The present SSA results (Table 1) could be explained on the basis of non-preservation of the cubic structure as will be discussed later on.

Fig. 1a presents powder XRD patterns obtained over the 50Mg-25Ce-25Zr-O (reference support), 40Mg-25Ce-25Zr-10La-O, 40Mg-20Ce-20Zr-20La-O, 40Mg-25Ce-25Zr-10Ba-O and 40Mg-25Ce-25Zr-10Zn-O mixed metal oxides, all prepared by the sol-gel method (Section 2.1). The following remarks are appropriate:

- (a) The diffraction peaks recorded at 42.5 and 62.3° 2 θ , which correspond to reflections from the (2 0 0) and (2 2 0) MgO lattice planes, are observed in the case of 50Mg-25Ce-25Zr-O support (reference), whereas they almost vanish in the case of doping with 10% La or 20% La. On the contrary, diffraction peaks corresponding to the (0 0 1) lattice plane of $\text{Mg}(\text{OH})_2$ phase are emerged at 18.98° and 18.6° for the 10% La- and 20% La-containing support, respectively. Exception to this

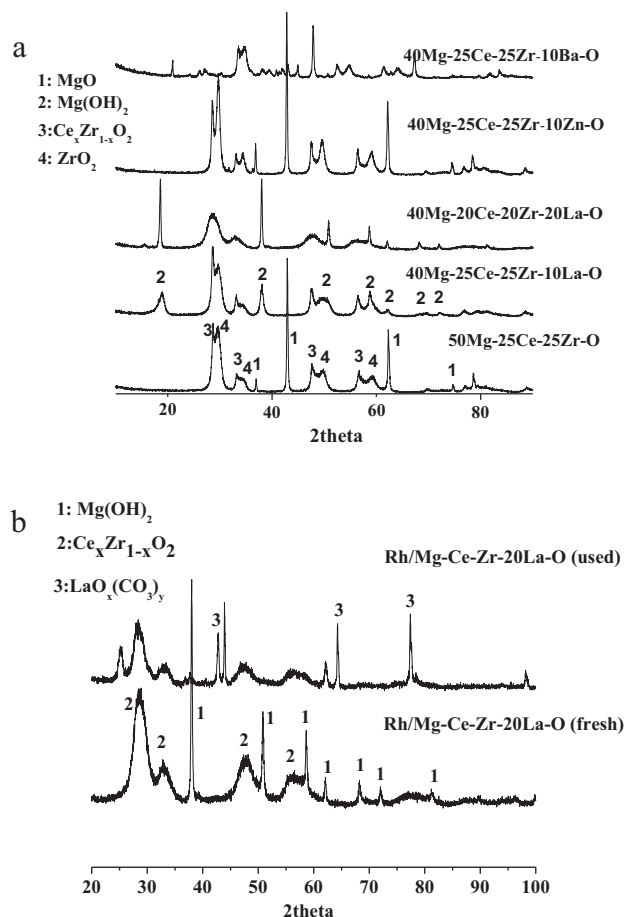


Fig. 1. Powder X-ray diffraction patterns of (a) 50Mg-25Ce-25Zr-O; 40Mg-25Ce-25Zr-10La-O; 40Mg-20Ce-20Zr-20La-O; 40Mg-25Ce-25Zr-10Zn-O; 40Mg-20Ce-20Zr-20Ba-O (fresh solids), and (b) 0.1 wt% Rh/40Mg-20Ce-20Zr-20La-O catalyst as fresh and after used for 24 h in phenol steam reforming reaction at 650 °C.

transformation of MgO to $\text{Mg}(\text{OH})_2$ appears in the case of Zn addition, which implies that Zn retards MgO hydroxylation. In the case of 10% Ba-containing support, the peak at 43.12° due to reflections from the (2 0 0) plane of MgO appears with very low intensity, whereas peaks corresponding to $\text{Mg}(\text{OH})_2$ appear as well.

- (b) A different shape for the peak recorded at 28.8°, which corresponds to the (1 1 1) reflection of cubic CeO_2 and/or $\text{Ce}_x\text{Zr}_{1-x}\text{O}_2$ solid solution was noticed. The asymmetry of this diffraction peak could be attributed to small distortions induced in the cubic fluorite lattice due to the introduction of Zr^{4+} (dopant) and the subsequent vacancy formation [44]. The identification of ZrO_2 peaks implies that Zr^{4+} was not fully introduced into the ceria cubic lattice. On the other hand, in the case of 40Mg-20Ce-20Zr-20La-O support, the (1 1 1) reflection of cubic fluorite is symmetric, and this could reflect the presence of a “true” solid solution, where La^{3+} ions are incorporated in a random way in the $\text{Ce}_x\text{Zr}_{1-x}\text{O}_2$ lattice, replacing Ce^{4+} cationic sites. This “true” solid solution could be understood by considering the facts that same atom % Ce, La and Zr elements (Ce:Zr:La = 20:20:20) were used in the synthesis, and the solubility of La_2O_3 in CeO_2 forming a cubic fluorite solid solution up to the composition of $\text{La}_{0.5}\text{Ce}_{0.5}\text{O}_{1.75}$ [45]. However, Mamontov et al. [46] reported in their inspiring work that diffraction patterns should be interpreted with caution, as they do not always reflect the real situation due to the intrinsic limitation of the technique. For example, in the case of $\text{Ce}_x\text{Zr}_{1-x}\text{O}_2$ materials,

two domains (2–3 nm) with different compositions can exist (e.g., a Ce-rich and a Zr-rich) but these cannot be probed by XRD as the structure and lattice orientation can be the same. In the same context, Montini et al. [47] reported on Eu(III) fluorescence spectroscopy results for probing the inhomogeneities of $\text{Ce}_x\text{Zr}_{1-x}\text{O}_2$ solid materials. The results of this technique proved to be complementary to those obtained using EXAFS. Based on the above, it should be considered that for the critical and unambiguous assessment of structural features of complex systems, several techniques besides XRD should be used.

- (c) By comparing the XRD patterns of 40Mg-25Ce-25Zr-10La-O and 40Mg-20Ce-20Zr-20La-O solids, a small shift in lower diffraction angles can be noticed in the case of 20% La-containing support. This can be explained based on the expansion of the lattice due to the increase of La content [44]; La^{3+} radius (1.36 Å) is larger than that of Ce^{4+} (0.97 Å) which introduces stress in the lattice.

Fig. 1b presents powder XRD profiles of the 20% La-containing catalyst before and after 24 h of phenol steam reforming at 650 °C. It is seen that the peak recorded at 28.6° 2θ due to (1 1 1) plane reflections of $\text{Ce}_x\text{Zr}_{1-x}\text{O}_2$ solid solution appeared with lower intensity in the case of used catalyst. Besides the decrease of its intensity, this peak appeared also to shift to a lower 2θ angle (28.2°), result that coincides with lattice rearrangements (e.g., expansion) and other disordering, closely related to the presence of O-vacancies in the support after phenol steam reforming. As reported by Balducci et al. [48], introduction of Zr^{4+} into the ceria lattice makes more energetically facile the $\text{Ce}^{4+} \rightarrow \text{Ce}^{3+}$ reduction in the stable (1 1 0) and (1 1 1) surfaces, whereas at the same time an increased segregation tendency of the oxygen vacancies to the aforementioned surfaces was noticed as Zr^{4+} concentration increased. Also, according to Mayer-nick and Janik [49], who studied the adsorption/activation of CH_4 on pure CeO_2 , Ce-Zr-O and Pd/ CeO_2 surfaces, methane adsorbs dissociatively leading to $^*\text{H}$ and $^*\text{CH}_3$, and the thermodynamics of this adsorption step is associated with that of oxygen vacancy formation over pure CeO_2 , Pd/ CeO_2 and mixed metal oxide Ce-Zr-O surfaces. Previous studies [50,51] showed that oxygen vacancies have a major role in steam activation for phenol steam reforming.

Based on the above discussion, the changes observed in the diffractogram of 20% La-containing supported Rh catalyst regarding the 28.6° peak, recorded before and after phenol steam reforming could be linked to Ce-sublattice changes. These are related to the (1 1 1) surface and bulk O-vacancies formation/filling, implying their vital role in the reaction. Another feature presented in Fig. 1b is that the intense peak recorded at 38° 2θ , corresponding to MgO periclase in the case of the fresh catalyst, has been replaced by a small peak, result indicating that some structural modification did take place during reaction. Other cation (Ce, Mg, La) sublattice changes, as can be traced by the XRD patterns of the solid after phenol steam reforming, thus indicating reorganization of support lattice, are the following:

- (a) In the case of 20% La-containing fresh catalyst, diffraction peaks at 38.1°, 50.7°, 58.6°, 62.0° and 68.2° 2θ appear. These are assigned to (1 0 1), (1 0 2), (1 1 0), (1 0 0) and (2 0 0) lattice planes of $\text{Mg}(\text{OH})_2$ phase, respectively. After phenol steam reforming, the peaks at 38.1°, 50.7°, and 58.6° have been reduced in intensity, and an increased FWHM was seen. According to Johnson et al. [52], MgO (1 0 0) plane is the one where dissociative than molecular adsorption of H_2O is more facile in terms of energy. Thus, it cannot be excluded the fact that MgO (1 0 0) has a major contribution in some of the important elementary steps of the reaction at hand, such as the generation of -OH species via water (steam) dissociation [50,51].

- (b) In the case of used 20% La-containing catalyst, the peak at 72.1° ($\text{Mg}(\text{OH})_2$ phase) disappears, and new peaks at 25.1°, 42.9°, 43.7°, 64.4° and 77.4° emerged, corresponding to the $\text{LaO}_x(\text{CO}_3)_y$ phase. These structural changes imply that phenol steam reforming at 650 °C induced support rearrangements due to the presence of steam, phenol, and/or reaction products (CO , CO_2 , H_2). The fact that the major structural changes are linked with Mg- and La-based phases (MgO , $\text{Mg}(\text{OH})_2$, La_2O_3) could possibly imply the predominant role of these basic oxide phases in specific aspects of phenol steam reforming, such as activation of phenol, surface regeneration, and promotion of the water gas shift reaction.
- (c) It is noteworthy to recall that in our previous studies [38,39] we have shown that when $\text{Ce}_x\text{Zr}_{1-x}\text{O}_2$ solid was treated with a 40% $\text{H}_2\text{O}/\text{He}$ gas stream at 655 °C for 3 and 24 h, its SSA was practically constant (within experimental error) with increasing steaming reaction time ($10 \text{ m}^2 \text{ g}^{-1}$ for 3 h vs. $9 \text{ m}^2 \text{ g}^{-1}$ for 24 h), while part of CeO_2 and ZrO_2 crystal phases was converted into cerium and zirconium hydroxide, respectively. Based on these results, it was concluded [38] that steam alone has practically no effect on the SSA of support but affects only the chemical composition of its crystal phases. Therefore, the changes observed in the SSA ($\text{m}^2 \text{ g}^{-1}$) and morphology of support after steam reforming of phenol must be assigned to the influence of phenol and its derived carbonaceous intermediates (e.g., C_xH_y , $\text{C}_x\text{H}_y\text{O}_z$), some of which accumulated on the support surface. XPS results presented in Section 3.6 corroborate this assumption.

3.1.2. Electron microscopy studies

Fig. 2a and b presents SEM photographs obtained over the 20% La- and 20% Ba-containing supports. These images corroborate for sponge-like textures. Fig. 3a presents HR-TEM picture obtained over the 10% La-containing solid, whereas the SAED pattern obtained over area II is shown in Fig. 3b. Similar studies were performed over the 20% La- and 10% Zn-containing solids, where the presence of the various phases identified by powder XRD had been confirmed. In particular, MgO forms layers that exist either alone or attached to larger particles that include other phases as well. All the phases observed were polycrystalline, as seen in the diffraction patterns of Fig. 3b. In general, ring patterns correspond to powder diffraction from multiple crystals with a variable orientation. The dashed dot texture presented in the SAED pattern (Fig. 3b) is typical for nanocrystalline material with no preferential orientation [53].

3.1.3. Redox behavior and thermal stability of Rh/Mg-Ce-Zr-X-O solids

3.1.3.1. H_2 -temperature-programmed reduction studies. Fig. 4 presents H_2 -TPR traces obtained on the 0.1 wt% Rh/40Mg-25Ce-25Zr-10X-O catalysts following calcination in 20% O_2/He at 750 °C for 2 h. According to previous studies [54,55], CeO_2 -containing mixed metal oxides exhibit H_2 -TPR traces characterized by three regions: (a) low-temperature reduction peak(s) (270–400 °C) corresponding to a surface reduction process [56,57]; (b) medium temperature (400–700 °C) reduction peak(s) corresponding to a reduction process linked with subsurface layers and deeper internal domains of nanoparticles; this area is dominated by high expansion of the lattice, whereas some chemical/structural irregularities could also be associated with; (c) high temperature reduction peak(s) ($T > 700$ °C) which is the fingerprint of bulk reduction.

The 0.1 wt% Rh/40Mg-25Ce-25Zr-10La-O catalyst presents a wide reduction profile in the 250–800 °C range. Two peaks with maxima at 540 and 690 °C appear which correspond to at least two different labile oxygen species originated from surface/subsurface and bulk layers of support, respectively. Furthermore, an

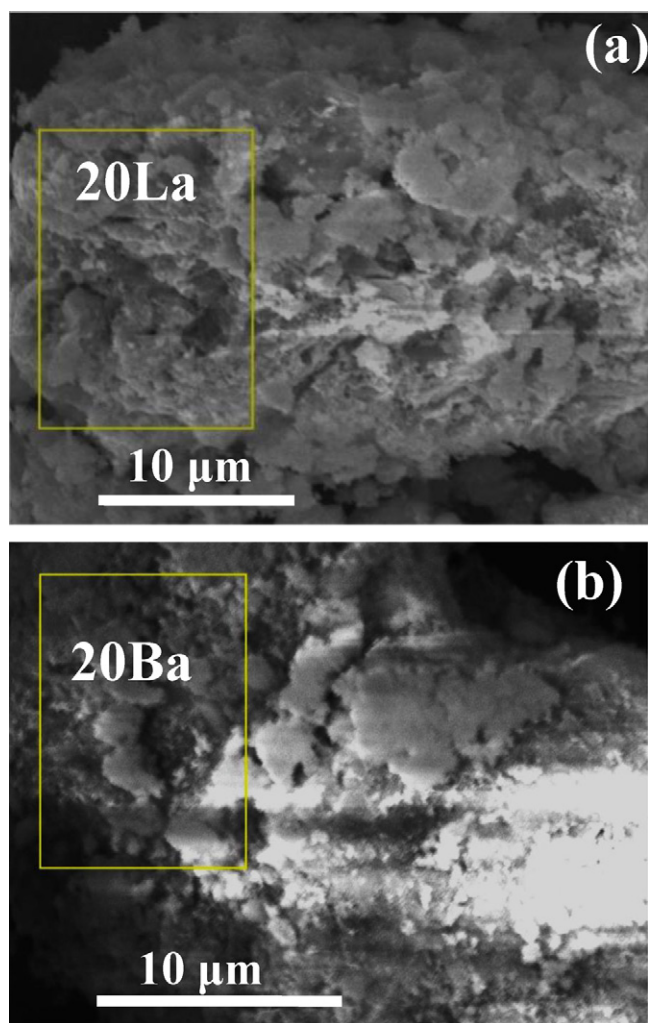


Fig. 2. SEM photograph of (a) 40Mg-20Ce-20Zr-20La-O and (b) 40Mg-20Ce-20Zr-20Ba-O solid supports (fresh).

additional small peak recorded at 190 °C appears, which corresponds to reduction of Rh_2O_3 particles, and likely of surface support species (Ce^{4+} , La^{3+}) in proximity with Rh_2O_3 [58]. The 0.1 wt% Rh/40Mg-25Ce-25Zr-10Zn-O catalyst presents a peak maximum at 460 °C corresponding to subsurface reduction of M–O–M' bonds with a broad tail out to 800 °C. In the case of 10% Ca- and 10% Sr-containing catalysts, reduction peaks at $T < 300$ °C, usually related to reduction of rhodium oxide or rhodium species at the metal–support interface were absent. This result strongly implies the impact of support chemical composition on the metal–support interactions, where in the present case of use of a low Rh loading (0.1 wt%) and particle size ($d_{\text{Rh}} < 2$ nm), these interactions are greatly facilitated. The 0.1 wt% Rh/40Mg-25Ce-25Zr-10Ba-O catalyst presents a broad reduction peak centered at 760 °C with a very broad shoulder on its rising part. This trace is attributed to different $\text{M}_1\text{–O–M}_2$ bonds in terms of electronic and chemical environment and less reducible oxygen species compared to the 10% La-containing catalyst. Reduction peak(s) of Rh_2O_3 and those associated with Rh oxide species at the metal–support interface are also included in the observed broad H_2 -TPR trace.

H_2 -TPR traces of 20% X-containing catalysts were also obtained (not shown here). In both cases (10% X- and 20% X-containing catalysts) it can be stated that addition of rare earth, alkaline-earth or transition metal oxide leads to a different extent of strengthening/weakening of the M–O–M and M–O–M' bonds regarding

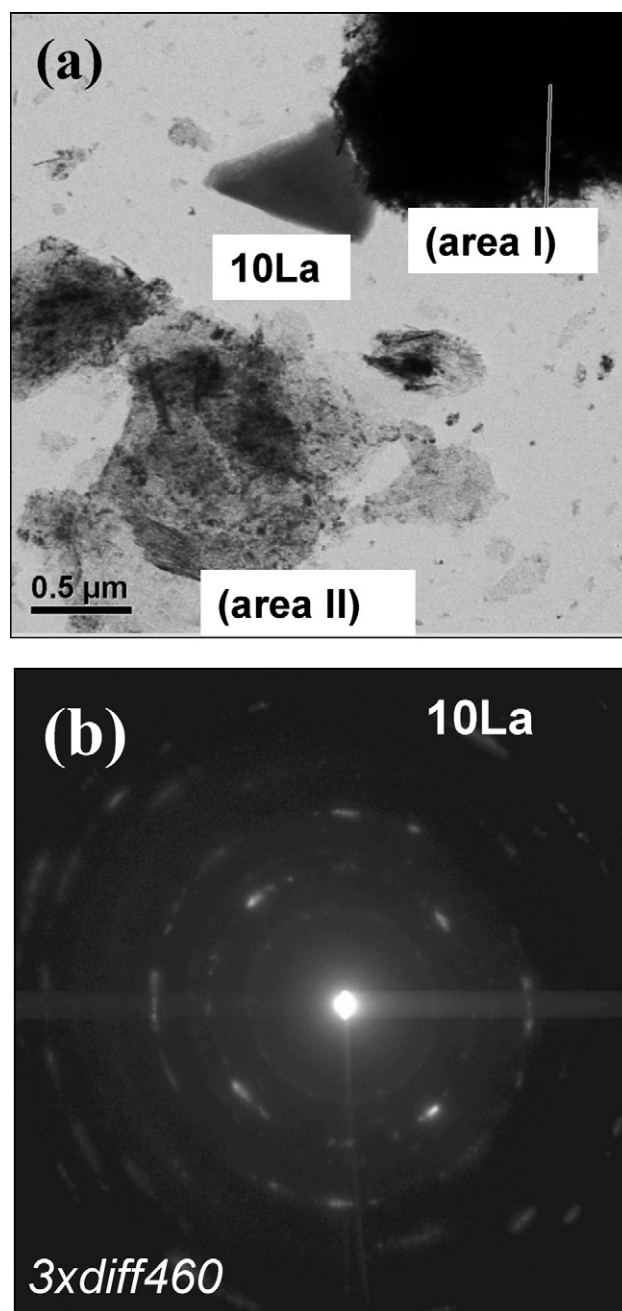


Fig. 3. (a) Transmission electron microscopy image of 40Mg-25Ce-25Zr-10La-O solid support; (b) selected area electron diffraction (SAED).

surface and bulk oxygen species. By integrating the H_2 -TPR traces, the amount of H_2 consumed and the corresponding amount of reducible oxygen can be estimated. Results are reported in Table 2 in terms of $\mu\text{mol O}$ per gram basis ($\mu\text{mol O/g}$) or per m^2 (based on SSA) of catalyst surface ($\mu\text{mol O/m}^2$). In the case of 0.1 wt% Rh/40Mg-25Ce-25Zr-10La-O, the obtained value of 545.9 $\mu\text{mol O/g}$ was the largest one among all catalysts investigated, while addition of 20% La in the support composition resulted in the largest concentration of labile oxygen per m^2 (Table 2). These results may imply the potential of these catalysts towards steam reforming of phenol, considering the significance of the presence of labile O/OH species in the reaction path [50,51].

After comparing the H_2 -TPR traces obtained (Fig. 4) and those of 20% X-containing solids (not shown), and based on the fact that bulk reduction of pure CeO_2 takes place at about 830 °C, and

Table 2

Concentration of labile oxygen species ($\mu\text{mol O/g}$ or $\mu\text{mol O/m}^2$) measured during H_2 -TPR over the 0.1 wt% Rh/Mg-Ce-Zr-X-O ($\text{X} = \text{La, Zn, Ca, Ba, Sr}$) catalysts.

Support chemical composition	$\mu\text{mol O/g}$	$\mu\text{mol O/m}^2$
50Mg-25Ce-25Zr-O	381.0	12.5
40Mg-25Ce-25Zr-10La-O	545.9	24.9
40Mg-25Ce-25Zr-10Zn-O	369.8	23.4
40Mg-25Ce-25Zr-10Ca-O	235.6	10.2
40Mg-25Ce-25Zr-10Ba-O	465.6	25.4
40Mg-25Ce-25Zr-10Sr-O	321.8	15.0
40Mg-20Ce-20Zr-20La-O	361.2	27.2
40Mg-20Ce-20Zr-20Ba-O	253.8	14.2
40Mg-20Ce-20Zr-20Zn-O	285.7	18.1
40Mg-20Ce-20Zr-20Ca-O	125.7	10.0
40Mg-20Ce-20Zr-20Sr-O	286.6	24.7

$\text{Ce}_x\text{Zr}_{1-x}\text{O}_2$ reduction is characterized by a broad H_2 -TPR trace, it can be concluded that the addition of divalent M^{2+} (Ca, Sr, Ba, Zn) or trivalent M^{3+} (La) cations induce structural disorders in the surface (low temperature peaks) and in the bulk (high temperature peaks) of the oxides. Another factor contributing to the different reduction behavior (Fig. 4) is the different solubility among the different metal oxides leading to an unavoidable wide dispersion in the local chemical environment of oxygen species. For instance, it has been reported that La_2O_3 forms a solid solution with CeO_2 up to a composition of $\text{La}_{0.50}\text{Ce}_{0.50}$ [45], whereas the solubility limit of CaO in CeO_2 is 4:1 [59]. Also, MgO solubility in CaO is reported to be $\sim 2\text{ wt\%}$, the solubility of CaO in MgO is $\sim 0.9\text{ wt\%}$ at 1620°C [60], and the solubility of SrO in CeO_2 is 9 wt\% [61]. It could be stated that bulk redox reactions occurring in these quaternary oxides have a pivotal role in the migration of oxygen vacancies. For instance, La_2O_3 addition seems to facilitate the surface to bulk mobility, likely through inducing a particular ordering in its structure, which in turn enhances anion vacancies migration, thus increasing ultimately the oxygen mass transport [62]. This is in harmony with previous work performed by us [25], where addition of 2–5 at.% Mg^{2+} ions enhanced OSC in the $350\text{--}550^\circ\text{C}$ range, and also the surface and bulk oxygen reducibility properties of the Mg-Ce-Zr-O solid. Vidmar et al. [63] also reported that La^{3+} addition in $\text{Ce}_x\text{Zr}_{1-x}\text{O}_2$ improves OSC of the final solid.

3.1.3.2. Structure evolution under redox gas atmosphere. Fig. 5a presents powder XRD spectra obtained over the 10% La-containing catalyst in the $300\text{--}700^\circ\text{C}$ range under the flow of a $20\% \text{O}_2/\text{Ar}$ gas mixture. For La-containing solids, it should be taken into account

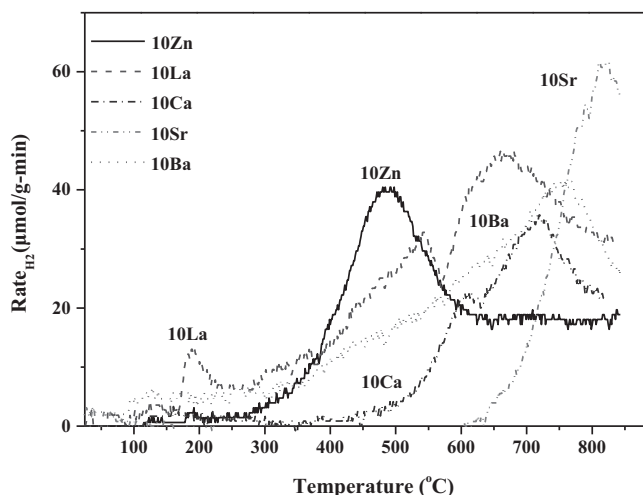


Fig. 4. H_2 -TPR profiles (H_2 consumption rate vs. T) obtained over the 0.1 wt% Rh/40Mg-25Ce-25Zr-10X-O catalysts ($\text{X} = \text{Ca, Zn, Ba, La, Sr}$).

that according to thermogravimetric analyses [64] performed in the $280\text{--}400^\circ\text{C}$ range, $\text{La}(\text{OH})_3 \rightarrow \text{LaOOH} + \text{H}_2\text{O}$ reaction takes place. In the $500\text{--}600^\circ\text{C}$ range, the reaction: $2\text{LaOOH} \rightarrow \text{La}_2\text{O}_3 + \text{H}_2\text{O}$ also takes place. For the XRD patterns presented in Fig. 5a, the following remarks are appropriate:

- The peak at 37.9° corresponding to the (101) lattice plane of $\text{Mg}(\text{OH})_2$ disappears after calcination at 400°C , implying that dehydroxylation occurs.
- At 300°C , a new peak at 43.3° appears, which is due to the $\text{La}(\text{OH})\text{CO}_3$ phase, whereas as the temperature is further increased the intensity of this peak is increasing, and another peak is emerged at 42.5° corresponding to the MgO (200) periclase phase.
- At the highest treatment temperature of 700°C , the intensity ratio ($I_{43.3}/I_{42.5}$) for the aforementioned diffraction peaks (point b) becomes close to unity, and the corresponding primary crystallite size is about 16 and 28 nm, respectively.

Treatment of the same catalyst in $20\% \text{H}_2/\text{He}$ gas atmosphere (Fig. 5b) had the following consequences: (a) the intensity of the peaks at 35.1° and 52.5° assigned to $\text{LaO}_x(\text{CO}_3)_y$ phase increases with increasing temperature (the same as in O_2 atmosphere); and (b) the intensity ratio of the peaks recorded at 42.8° and 43.1° which correspond to MgO and $\text{LaO}_x(\text{CO}_3)_y$ phases, respectively, changes with temperature.

Based on the full width at half maximum (FWHM) analysis and the Scherrer equation: $D = 0.9\lambda/\beta \cos \theta$ [65], where λ is the X-ray wavelength (0.15418 nm), and β is the full-width at half-maximum intensity of the diffraction line, the primary crystallite size of the associated phase can be estimated under oxidative or reducing gas atmosphere, and these results are shown in Fig. 5c and 5d, respectively. The main conclusion is that the mean primary crystal size of $\text{LaO}_x(\text{CO}_3)_y$ and MgO phases present in the 40Mg-25Ce-25Zr-10La-O solid (Fig. 5a and b) decreases with increasing temperature in the $300\text{--}600^\circ\text{C}$ range under O_2/Ar gas atmosphere, whereas at 700°C a slight increase is noted due to sintering. On the other hand, the particle size of $\text{Ce}_x\text{Zr}_{1-x}\text{O}_2$ solid increases from 300 to 400°C and follows a very similar pattern with a further increase of temperature as that exhibited by the other two phases. The $\text{Ce}_x\text{Zr}_{1-x}\text{O}_2$ crystallites exhibit a decrease in size from 18 to 13 nm with increasing temperature in the $400\text{--}600^\circ\text{C}$ range, and even though this seems to be contradictory with the lattice expansion of $\text{Ce}_x\text{Zr}_{1-x}\text{O}_2$ by La^{3+} addition, it could be associated with the partial La^{3+} ion migration into the Ce-Zr-O lattice and the well ordering of the lattice. This could lead to cell shrinkage and increase of thermal stability [59] and/or more Zr^{4+} incorporation into $\text{Ce}_x\text{Zr}_{1-x}\text{O}_2$, which would lead to lattice contraction, both being temperature driven phenomena. It is noted that there is no solid solubility of CeO_2 in La_2O_3 [45], and this could possibly lead to La^{3+} migration out of $\text{Ce}_x\text{Zr}_{1-x}\text{O}_2$ as temperature increases, thus contributing to a temperature induced size reduction as previously discussed. For $T > 400^\circ\text{C}$, the particle size decreases since more Zr^{4+} is incorporated into the CeO_2 lattice, leading to a more homogeneous solid solution with better resistance to sintering [43,66].

Under H_2/Ar gas atmosphere a systematic increase of the primary crystallite size is obtained for $\text{Ce}_x\text{Zr}_{1-x}\text{O}_2$ and $\text{LaO}_x(\text{CO}_3)_y$, whereas for MgO the crystallites appear to be rather stable in agreement with literature [67]. Sieger et al. [68] studied the thermal stability of nanocrystalline Sm_2O_3 and $\text{MgO-Sm}_2\text{O}_3$ and reported that the mixed oxide exhibited an enhanced microstructural stability compared with the single oxide of Sm_2O_3 . This was due to the fact that Sm_2O_3 and MgO grains were found separated since no solid solution between the two phases can be formed, and grain growth is predominantly driven by surface diffusion which is suppressed because each phase serves as diffusion barrier for the other.

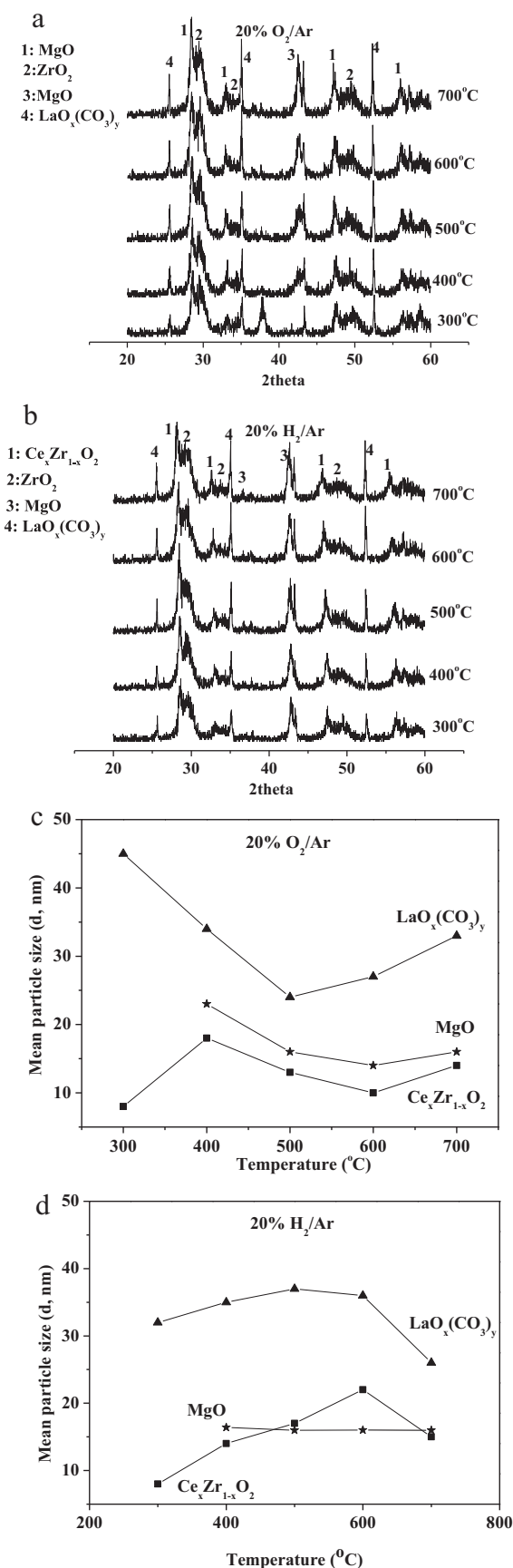


Fig. 5. *In situ* powder X-ray diffraction patterns recorded over the 40Mg-25Ce-25Zr-10La-O catalyst support in the flow of 20% O₂/Ar gas mixture in the 300–700 °C range (a) followed by 20% H₂/Ar gas mixture treatment in the same temperature range (b);

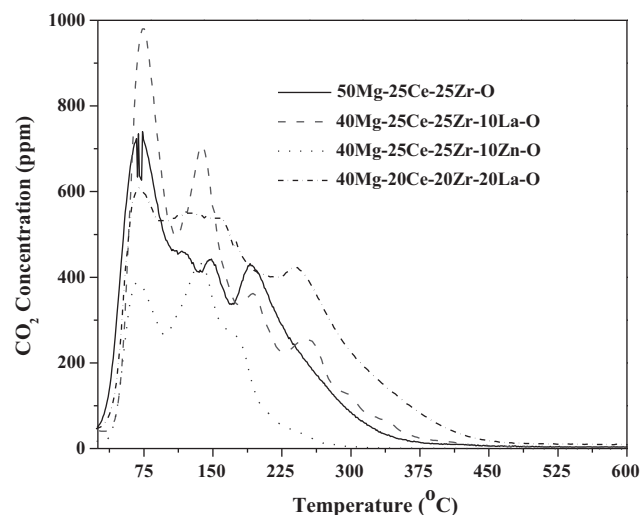


Fig. 6. CO₂-TPD profiles obtained over the 50Mg-25Ce-25Zr-O, 40Mg-25Ce-25Zr-10La-O, 40Mg-25Ce-25Zr-10Zn-O, and 40Mg-20Ce-20Zr-20La-O solid supports. W = 0.2 g; Q = 30 NmL/min; β = 30 °C/min.

It is speculated whether the aforementioned mechanism operates for the present case between MgO and Ce_xZr_{1-x}O₂ or LaO_x(CO₃)_y.

In the case of Ce_xZr_{1-x}O₂ crystallites, a more pronounced size increase is seen with increasing temperature in H₂/Ar treatment, and this is linked with the reduction of Ce⁴⁺ (1.01 Å) to Ce³⁺ (1.143 Å) [69]. Sohlberg et al. [70] studied the interaction of H₂ with CeO₂ and they reported that hydrogen atoms entering the bulk of ceria lead to a hydroxyl group formation, where this ultimately causes a slight expansion of the cubic lattice. Rohart et al. [43] studied the thermal stability of Ce_xZr_{1-x}O₂ mixed oxides in the whole compositional range, and reported that by effectively controlling morphology at micro and macro domains particle's sintering under harsh ageing conditions can be avoided. Liu et al. [71] and Malakhov and Samsonov [72] stated that thermal stability is a complex phenomenon that is related to factors such as ionic radius, electronic configuration (d, f shells), and principal quantum number.

3.1.4. Acidity/basicity and its correlation to the steam reforming reaction

Fig. 6 presents TPD-CO₂ profiles over the 50Mg-25Ce-25Zr-O, 40Mg-25Ce-25Zr-10La-O, 40Mg-25Ce-25Zr-10Zn-O and 40Mg-20Ce-20Zr-20La-O solids. By comparing the TPD-CO₂ profile obtained over the Mg-Ce-Zr-O solid (reference support), and the ones obtained over the modified supports, it can be stated that La³⁺ addition (10 and 20 at.%) led to a redistribution of basic sites. In particular, an increase in the concentration of stronger basic sites appears, where a new peak emerged at 260 °C, result that could be associated with the superior catalytic performance of the respective supported Rh, as will be discussed later. It is known that the enhancement of support basicity leads to the promotion of carbon gasification (e.g., C + H₂O ↔ CO + H₂), and as a consequence of that the increase in -OH species concentration on the surface [15,24,25]. The latter species migrate onto the metal, where they participate in reactions with hydrocarbon fragments towards CO, CO₂ and H₂ formation [50,51,73]. The efficiency of the catalyst to self-sustain its activity through the participation of labile O/OH species of support towards oxidation of the accumulated carbon is of great importance for the sustainable durability of the reforming catalyst [74].

Mean particle size of MgO, Ce_xZr_{1-x}O₂ and LaO_x(CO₃)_y phases obtained under 20% O₂/Ar gas mixture (c) and 20% H₂/Ar gas mixture (d) as a function of treatment temperature.

Table 3

NH₃ and CO₂ uptakes (μmol/g) measured during TPD studies on the Mg-Ce-Zr-X-O (X=La, Zn, Ba) mixed metal oxide supports investigated. The ratio of acid to basic sites (ψ) as a function of support chemical composition is also reported.

Support chemical composition	NH ₃ (μmol/g)	CO ₂ (μmol/g)	Acid/basic site ratio (ψ)
50Mg-25Ce-25Zr-O	114.8	28.8	3.9
40Mg-25Ce-25Zr-10La-O	221.1	32.2	6.8
40Mg-25Ce-25Zr-10Zn-O	96.2	15.8	6.0
40Mg-20Ce-20Zr-20La-O	333.7	37.3	8.9
40Mg-20Ce-20Zr-20Ba-O	92.2	28.0	3.3

Table 3 presents results of basicity (CO₂-TPD) and acidity (NH₃-TPD) measurements performed on five mixed metal oxides used as supports of Rh investigated. The surface basicity was found to increase by La-modification of the Mg-Ce-Zr-O mixed metal oxide. In particular, the support containing 20 at.% La exhibits the highest concentration of basic sites, result that coincides with the best catalytic behavior of 0.1 wt% Rh/Mg-Ce-Zr-20La-O solid (Section 3.3). The values reported in Table 3 are in good agreement with results reported by Kabner and Baerns [75] on the basicity of different rare earth oxides. They found that La₂O₃-CaO and CeO₂-CaO systems exhibited the highest surface acidities. Constantinou and Efsthathiou [26] reported on a Ce_xZr_{1-x}O₂ solid solution modified by 2–5 at.% Mg. They reported that by increasing the Mg²⁺ content from 2 to 5 at.% but keeping the Ce/Zr ratio constant, more intense CO₂ desorption profiles are obtained. The authors concluded that the concentration and strength of basic sites increased by Mg²⁺ addition. In the present case, it could be stated that Lewis-type basic centers (Oⁿ⁻) are likely subjected into a redistribution of their electron density by adding different ions (La³⁺, Sr²⁺, Ba²⁺, Ca²⁺, Zn²⁺) in their coordination sphere, leading thus to different CO₂ desorption profiles.

Regarding the surface acidity of the five solids listed in Table 3, it is seen that this increases significantly by La-modification of the Mg-Ce-Zr-O mixed metal oxide. Addition of 10 and 20 at.% La in the Mg-Ce-Zr-O oxide causes an increase of surface acidity by a factor of 1.9 and 2.9, respectively. The addition of new metal cations acting as Lewis acid centers could support the fact that the observed acidity on these materials is largely of Lewis-type (Mⁿ⁺ ions) [75]. The ratio of acid to basic sites (ψ) as determined by NH₃ and CO₂ chemisorption is also reported in Table 3. It is seen that La³⁺ addition causes this parameter to increase significantly with respect to the reference 50Mg-25Ce-25Zr-O material. On the other hand, addition of Ba²⁺ causes this parameter to take a lower value (ψ = 3.3 vs. 3.9, Table 3).

3.2. Structure evolution under simulated reaction conditions

Fig. 7 presents powder XRD patterns recorded *in situ* under a simulated H₂/CO/CO₂ gas product of phenol steam reforming as a function of treatment temperature over the (a) 10% La-, (b) 10% Zn-, and (c) 20% La-containing supported Rh (0.1 wt%) catalysts. The diffraction patterns of 10% La-containing support shows that the peak at 37° 2θ (Mg(OH)₂) is preserved contrary to the case of the same solid under 20% O₂/He gas treatment (Fig. 5). The peak at 43.3° 2θ (La(OH)CO₃) appears intense and sharp as opposed to the case under the 20% O₂/He gas treatment (Fig. 5). This could be due to the partial decomposition of the carbonate phase under oxidative gas atmosphere, contrary to the sustainable growth of this phase under H₂/CO/CO₂ gas atmosphere. By comparing the intensity of the two coupled peaks recorded at 42.6° and 43.3° 2θ (MgO and La(OH)CO₃ phases, respectively), it can be stated that their intensity ratio is about unity under the oxidative gas atmosphere (Fig. 5a), whereas it far exceeds unity as temperature increases under H₂/CO/CO₂ gas treatment. This corroborates the assumption of carbonate-related

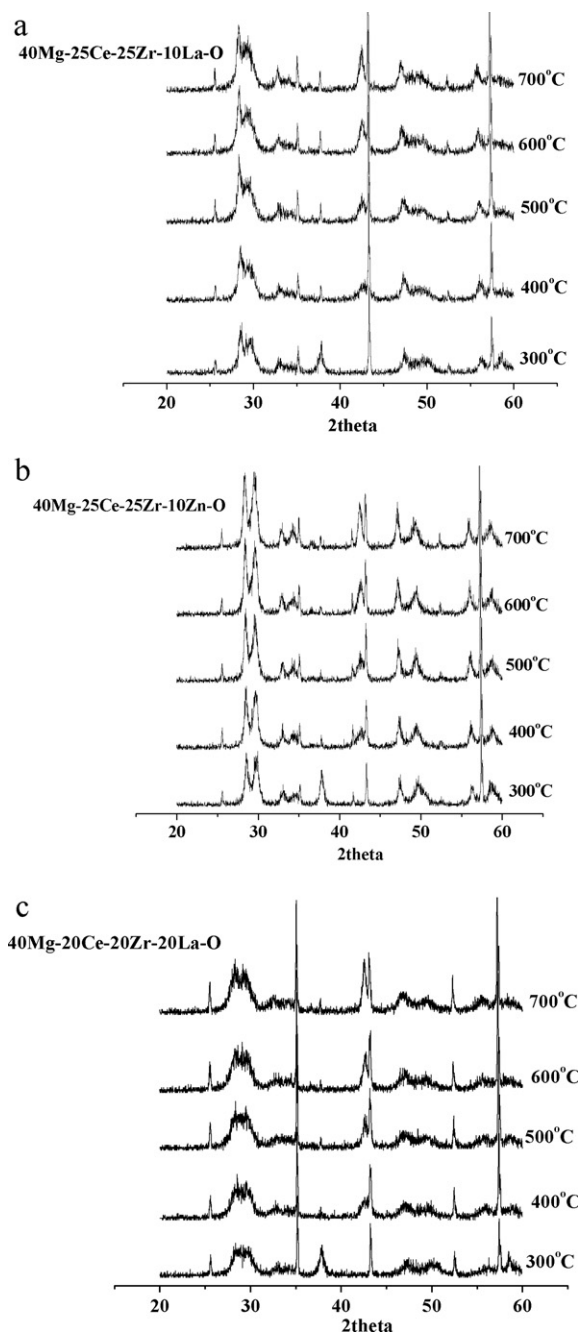


Fig. 7. *In situ* powder X-ray diffraction patterns recorded over the 40Mg-25Ce-25Zr-10La-O (a), 40Mg-25Ce-25Zr-10Zn-O (b) and 40Mg-20Ce-20Zr-20La-O (c) solids in the flow of a 5% H₂/5% CO/5% CO₂/He gas mixture as a function of treatment temperature (300–700 °C).

phase(s) formation under steam reforming reaction (575–730 °C). Also, the peak at 52.5° 2θ (LaO_x(CO₃)_y) appears with low intensity under H₂/CO/CO₂ gas treatment, whereas under O₂/Ar and H₂/Ar gas treatments it appears more intense with a larger intensity under the O₂/Ar gas treatment (Fig. 5). Based on these results, it could be stated that the LaO_x(CO₃)_y phase is more thermally stable under the 20% H₂/Ar reducing gas atmosphere, and its formation growth or reaction is inhibited under the H₂/CO/CO₂ gas atmosphere.

By comparing the XRD patterns of 10% La- and 20% La-containing solids under H₂/CO/CO₂ gas atmosphere (Fig. 7a and c), the following are noted: (a) The peaks at 28.5° and 29.6° 2θ (Ce_xZr_{1-x}O₂ solid solution and ZrO₂, respectively) appear with higher intensity and more well resolved in the case of 10% La-containing solid. The

less crystalline nature (or crystalline solid with particles sizes that escape XRD detection), and the possible formation of a more homogeneous $\text{Ce}(\text{La})_x\text{Zr}_{1-x}\text{O}_2$ solid solution appeared in the case of 20% La-containing solid are the main reasons for that. (b) The former two diffraction peaks are less intense under H_2/Ar gas treatment, implying the major impact of O_2/Ar and $\text{H}_2/\text{CO}/\text{CO}_2$ gas treatments in the crystalline growth of this particular phase.

In the case of 10% Zn-containing solid (Fig. 7b), the two coupled peaks at 28.3° and 28.7° 2θ appear with higher intensity, and are also more well resolved compared with the ones observed in the other two solids. The same is true for the peaks recorded at 42.62° and 43.1° 2θ attributed to MgO and $\text{LaO}_x(\text{CO}_3)_2$, respectively. The peak at 50° 2θ is much more intense in the case of 10% Zn-containing solid than in the other two solids. The more crystalline nature of phases in the 10% Zn-containing solid compared to the La-containing ones could be associated with the likely lower thermal stability of the latter as evidenced by the results shown in Fig. 5c and d.

3.3. Catalytic performance studies

Fig. 8a presents the hydrogen yield (%) obtained in the $575\text{--}730^\circ\text{C}$ range over the various supported Rh catalysts (0.1 wt% Rh), where the supports belong to the 10% X series. The catalysts with 10% La and 10% Ba present the best performance compared with the other solids, in particular the 10% La in the $650\text{--}730^\circ\text{C}$ range. It should be stated here that among the rare earth and alkaline-earth metal additives, La and Ba are the ones that caused the highest basicity (Table 3), in agreement also with the literature [76]. This result along with the H_2 -TPR studies (Fig. 4) which showed that 10% La- and 10% Ba-containing solids exhibit the largest concentration of labile oxygen species, namely 546 and $466\ \mu\text{mol O/g}$, or 24.9 and $25.5\ \mu\text{mol O/m}^2$, respectively, suggests for the partial contribution of surface basicity to the increased rate of phenol steam reforming over the respective supported Rh catalysts.

Fig. 8b presents the H_2 yield (%) obtained in the $575\text{--}730^\circ\text{C}$ range over the same supported Rh catalysts where the supports belong to the 20% X series. It is clearly seen that the 20% La-containing catalyst exhibits the best behavior in the whole temperature range, providing significantly larger H_2 yield (%) values than the reference (0.1 wt% Rh/50Mg-25Ce-25Zr-O) and Ni-based commercial catalysts. It is recalled that the 20% La-containing catalyst exhibits the highest concentration of labile oxygen species ($361.2\ \mu\text{mol O/g}$ or $27.2\ \mu\text{mol O/m}^2$, Table 2) among the 20% X-containing catalysts, and also the highest concentration of basic sites (Table 3). For the highest H_2 yield (%) observed on the Rh/40Mg-20Ce-20Zr-20La-O solid, the phenol conversion was in the $88\text{--}95\%$ range ($575\text{--}730^\circ\text{C}$, Fig. 8b).

Fig. 9a presents the effect of support chemical composition on the CO/CO_2 gas product ratio. According to the main network of reactions (1) and (2), the CO/CO_2 product ratio is determined by the relative rates of these reactions, and in most of the cases this ratio was found to decrease with increasing reaction temperature. This could be explained by considering that either the WGS reaction is kinetically controlled or a decrease in the number of active sites responsible for the formation of CO occurs in the $575\text{--}730^\circ\text{C}$ range. The latter could be partly related to “carbon” formation as evidenced at 655 and 700°C (see Section 3.4). In general, the 20% X-containing catalysts present lower CO/CO_2 ratios than the corresponding 10% X-containing ones. In the case of 20% La-containing catalyst, this ratio is more than two times lower compared with the 20% Ba-containing catalyst (Fig. 9b). The latter can be understood after considering the fact that WGS reaction activity is largely enhanced over catalysts with higher concentration of labile oxygen [77], in harmony with the fact that the present 20% La- and 20%

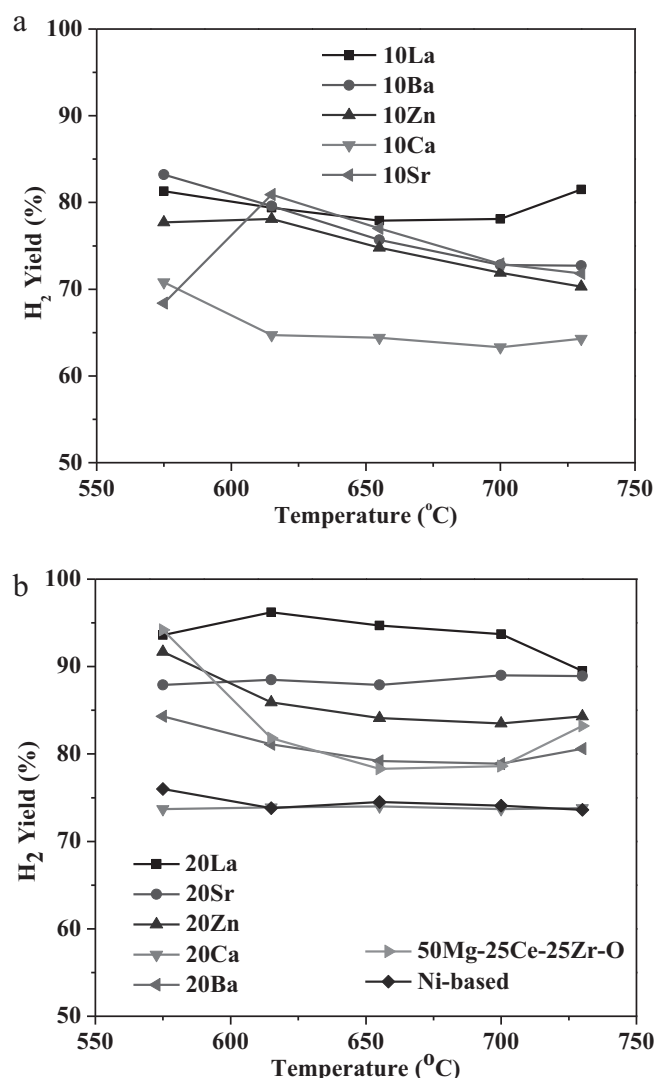


Fig. 8. Effect of support chemical composition on the H_2 yield obtained over the 0.1 wt% Rh/40Mg-25Ce-25Zr-10X-O (a) and 0.1 wt% Rh/40Mg-20Ce-20Zr-20X-O (b) (X = La, Ba, Zn, Ca, Sr) catalysts in the $575\text{--}735^\circ\text{C}$ range. Reaction conditions: $0.5\% \text{C}_6\text{H}_5\text{OH}/40\% \text{H}_2\text{O}/\text{He}$; $t = 30$ min; $W = 0.3$ g; $F_T = 200$ Nml/min; $\text{GHSV} = 80,000\ \text{h}^{-1}$. In (b) results are shown for the 0.1 wt% Rh/50Mg-25Ce-25Zr-O and commercial Ni-based catalysts.

Ba-containing catalysts present 361 and $254\ \mu\text{mol O/g}$ of labile oxygen (Table 2).

Fig. 10 presents comparative results of the integral specific rate of H_2 production ($\mu\text{mol H}_2/\text{m}^2\ \text{min}$) as obtained over the best sol-gel synthesized Mg-Ce-Zr-X-O supported Rh solids. For comparison purposes, the 0.1 wt% Rh/50Mg-25Ce-25Zr-O catalyst (reference) performance is also presented. It is clearly seen that addition of 20 at.% La led to a significant increase in the phenol steam reforming specific reaction rate (an increase by a factor of about two), while addition of Ca resulted in a significant deterioration of activity. These results are important since it is proved that the conceptual design of these MgO-based supported Rh catalysts and their tailored synthetic approach applied was successful. It is also important to mention that the Rh mean particle size (estimated through H_2 chemisorption at 25°C followed by TPD) in all the supported 0.1 wt% Rh catalysts (Table 1) was in the $1.5\text{--}1.7$ nm range, suggesting that the trend of activity behavior shown in Fig. 10 would be the same if TOF (s^{-1}) were to be estimated for specific activity evaluation.

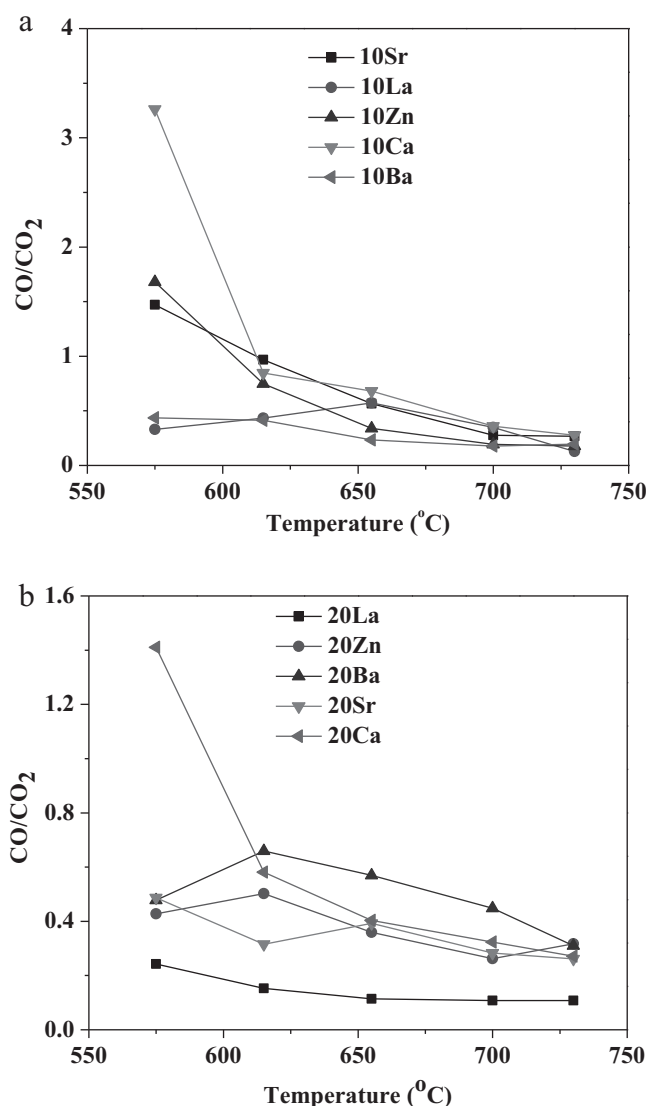


Fig. 9. Effect of support chemical composition on the CO/CO₂ gas product ratio over the 0.1 wt% Rh/40Mg-25Ce-25Zr-10X-O (a) and 0.1 wt% Rh/40Mg-20Ce-20Zr-20X-O (b) (X = La, Ba, Zn, Ca, Sr) catalysts in the 575–735 °C range. Reaction conditions: 0.5% C₆H₅OH/40% H₂O/He; $t = 30$ min; $W = 0.3$ g; $F_T = 200$ NmL/min; GHSV = 80,000 h⁻¹.

It is worthwhile to mention here that the reaction mechanism of steam reforming of toluene over supported Rh, Pd, and Pt consists of two important mechanistic paths [78,79]. In the first one, toluene is primarily dissociated on the noble metal leading to adsorbed hydrocarbon fragments. In the second path, water adsorption and dissociation occur mainly on the support surface. The resulting –OH groups migrate onto the metal particles through the metal–support interface. Once on the metal, they react rapidly with hydrocarbon fragments to give CO, CO₂ and H₂. The above described reaction paths have also been adopted to explain the steam reforming of other aromatic compounds [15,80] and that of phenol over Ni-based catalysts [30]. For the present supported Rh catalysts, Rh activates phenol, namely the O–H, –CH₂– and –C–C– entities, and promotes the reaction of C_xH_y fragments derived with the OH/O species present in the mixed metal oxide support. According to our previous work [50,51] on phenol steam reforming over supported Rh and Fe/Mg–Ce–O catalysts, the back-spillover of labile O/OH species from the support to the metal–support interface was proven as a fundamental mechanistic step towards H₂, CO and CO₂

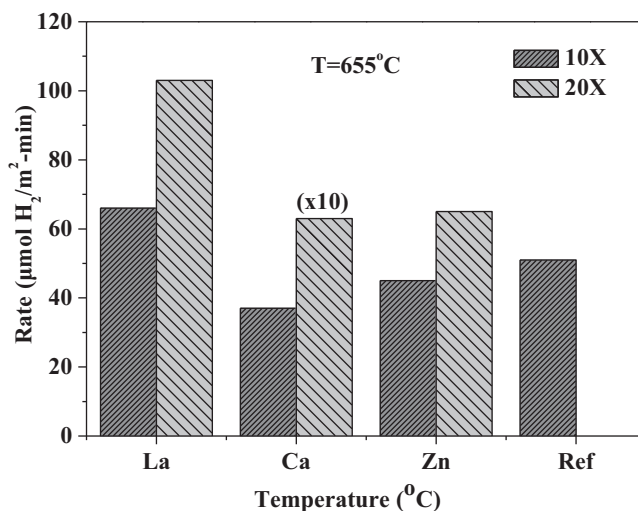


Fig. 10. Effect of support chemical composition on the specific integral rate of H₂ production (μmol H₂/m² min) obtained at 655 °C for the best sol–gel synthesized catalysts: 0.1 wt% Rh/Mg–Ce–Zr-10X(20X)-O (X = La, Ca, and Zn). Reaction conditions: 0.5% C₆H₅OH/40% H₂O/He; $t = 30$ min; $W = 0.3$ g; $F_T = 200$ NmL/min; GHSV = 80,000 h⁻¹. The performance of the reference catalyst (Ref. = 0.1 wt% Rh/50Mg-25Ce-25Zr-O) is also shown.

product formation based on various transient isotopic experiments performed.

In an effort to better understand the effect of support composition on the activity of the present supported Rh catalysts (Figs. 8–10), the following should be considered:

- Based on the H₂-TPR studies, addition of 10–20 at.% La³⁺ in the Mg–Ce–Zr–O support composition resulted in a lowering of binding energy of surface oxygen (M–O–M and M–O–M' entities).
- Based on the CO₂-TPD studies, it is concluded that La³⁺ addition increased the number of surface basic sites (Oⁿ⁻) per gram basis. It is well known [15] that support basicity enhances water dissociation leading to –OH species formation. As previously discussed, this species is of vital importance for the reaction at hand. Another beneficial role of basic sites as illustrated by *in situ* DRIFTS studies [26] is that they influence the WGS reaction rate, an important route in the phenol steam reforming reaction network (Eqs. (1) and (2)). In particular, after performing DRIFTS–CO experiments [26] it was shown that the support chemical composition affects the kinds and relative population of adsorbed CO on Rh; CO is a product of phenol steam reforming reaction. A larger concentration of active formate species was also reported in the case of Rh/Mg–Ce–Zr–O compared to the Rh/Ce–Zr–O catalyst [26].
- As shown in Fig. 9, the catalyst containing 20% La presents the lowest CO/CO₂ ratio. This result agrees very well with that reported by Constantinou and Efstathiou [26], where the best performing catalyst showed the lowest CO/CO₂ product ratio; this was partially linked to the higher concentration of cationic Rhⁿ⁺ species present in the specific catalyst [26]. According to the XPS results to be presented in Section 3.6, a significant percentage of Rh in the used Rh/Mg–Ce–Zr-10La–O catalyst appears in the Rhⁿ⁺ oxidation state. In the case of ethanol steam reforming [81], the CO/CO₂ gas product ratio was reported to be very sensitive to the Ce/Zr ratio in the Rh/Ce–Zr–O catalysts.

The above offered discussion could be further highlighted by bearing in mind the following intrinsic properties of alkaline-earth, rare earth and transition metal oxides/carbonates:

- Among the alkaline-earth metal oxides, surface basicity follows the order $\text{BaO} > \text{SrO} > \text{CaO} > \text{MgO}$ [82]. The stability of surface carbonates is directly correlated with the basicity of the corresponding metal oxide, and thus follows the order: $\text{BaCO}_3 > \text{SrCO}_3 > \text{CaCO}_3 > \text{MgCO}_3$ [82,83]. It was found [84] that carbonates formation suppresses OSC of the oxidic support, leading to progressive catalyst deactivation.
- Among the rare earth oxides (REO), lanthana is the one which exhibits the highest surface basicity [85].
- Basic sites promote dehydration, whereas acid sites dehydrogenation, thus leading to different carbonaceous intermediates (e.g., C_xH_y species) onto the catalyst surface. Thus, the relative concentration of acid and basic sites on the surface (Table 3) plays an important role in regulating the final product distribution obtained.
- Based on the present XRD studies, the solid supports with composition 40Mg-25Ce-25Zr-10La-O and 40Mg-20Ce-20Zr-20La-O preserve the fluorite cubic structure, thus high concentrations of labile oxygen as illustrated in the work of Fornasiero et al. [86].
- It has been reported that the reactivity order of $\text{Ba} > \text{Ca} > \text{Mg}$ in the case of soot combustion could be directly related to the peroxide and/or superoxide formation [87]. This means that different supports facilitate the formation of different reactive oxygen species, as illustrated by the present H_2 -TPR studies (Fig. 4). Abdel Halim and Shalabi [88] have studied the stability of peroxide ion O_2^{2-} on MgO, CaO and SrO surfaces, and reported that the stability of peroxy bond increases in the order: $\text{MgO} < \text{CaO} < \text{SrO}$.
- Regarding the $\text{Ce}_x\text{Zr}_{1-x}\text{O}$ phase of support, the Lewis acid strength decreases from CeO_2 to $\text{Ce}_x\text{Zr}_{1-x}\text{O}_2$. For the latter solid, surface O^{2-} basic sites lead to carbonates formation. Under steam reforming reaction the formation of carbonates has been reported [26]. In the present work, carbonates formation was proved using *in situ* XRD under 5% H_2 /5% CO /5% CO_2 gas atmosphere (Fig. 6). It has been observed that population of carbonate species increases as Ce^{4+} content increases since the latter facilitates the incorporation of CO_2 around Zr^{4+} ions [89].

3.4. Characterization of carbonaceous species formed during phenol steam reforming

Fig. 11 shows transient isothermal response curves of gaseous CO , H_2 and CO_2 obtained following the switch $\text{C}_6\text{H}_5\text{OH}/\text{H}_2\text{O}/\text{He}$ (T , 3 h) \rightarrow He (15 min) \rightarrow 40% $\text{H}_2\text{O}/\text{He}$ (T , t) over the 0.1 wt% Rh/40Mg-20Ce-20Zr-20La-O catalyst, where $T = 655^\circ\text{C}$ (Fig. 11a) or 755°C (Fig. 11b). During the 40% $\text{H}_2\text{O}/\text{He}$ gas switch, steam reacts with the carbonaceous deposits forming CO_2 , CO and H_2 . The amounts of CO_2 , CO and H_2 were estimated by integrating the respective response curves obtained after completion of the surface reaction of carbonaceous species with steam (until no CO/CO_2 was observed). The total amount of equivalent “carbon” reacted off as CO and CO_2 was found to be 7.3 mmol C/g at 655°C and 4.0 mmol C/g at 755°C .

A TPO experiment performed on the same catalyst (Section 2.4) provided lower amounts (~ 10 times) of carbonaceous deposits reacting under an oxygen gas atmosphere. These results illustrate the beneficial effect of steam in removing carbonaceous deposits formed during phenol steam reforming over the present supported Rh catalysts. It should be considered here that before performing the TPO experiment, the catalyst was thermally treated up to 800°C in He flow in order to decompose any carbonates formed under phenol steam reforming. This treatment could lead to structural and textural changes of the catalyst given that the initial catalyst pretreatment was done at a lower temperature (600°C , Section 2.1). It is known that ceria-related materials having relatively low surface areas are prone to sintering at temperatures higher than 500°C [90].

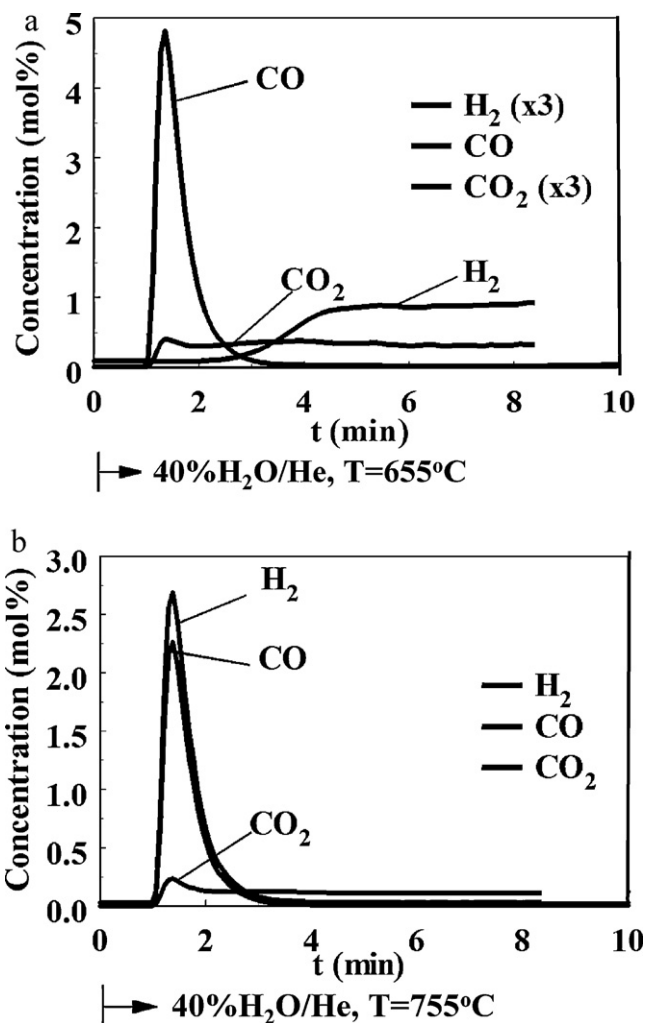


Fig. 11. Characterization of “carbon” deposits on the 0.1 wt% Rh/40Mg-20Ce-20Zr-20La-O catalyst after phenol steam reforming. Gas delivery sequence: 0.5% $\text{C}_6\text{H}_5\text{OH}/40\% \text{H}_2\text{O}/\text{He}$ (T , 3 h) \rightarrow He (755°C , 15 min) \rightarrow 40% $\text{H}_2\text{O}/\text{He}$ (755°C , t). (a) $T = 655^\circ\text{C}$; (b) $T = 755^\circ\text{C}$; $W = 0.3$ g.

Also, during carbonates decomposition and water evolution under He treatment at 800°C , the resultant CO_2 and H_2O might facilitate carbon gasification, thus potentially leading to an underestimation of the quantity of carbon formed during phenol steam reforming.

As reaction temperature increases, rearrangement of the carbonaceous skeleton ($-\text{C}_x\text{H}_y$) and loss of hydrogen atoms become more intense [91]. From the results of Fig. 11, an average H/C compositional ratio of carbonaceous deposits can be estimated. This is found to be 2.3 and 0.9 at 655 and 755°C , respectively, showing that, when phenol steam reforming takes place at higher temperatures, the carbonaceous deposits formed have a more H-deficient chemical composition.

3.5. Catalyst stability

Fig. 12 presents results of the stability in terms of H_2 production with time on stream at 700°C of three of the supported Rh catalysts developed, namely 10% La-, 20% La- and 10% Zn-containing catalysts. It is clearly seen that there is about 15–20% increase in hydrogen production within the first 2 h on stream for all the catalytic runs. In the case of 10% La-containing catalyst, between 2 and 5 h on stream H_2 production decreases, while after that, and up to 24 h on stream, there is a continuous increase in H_2 production; a 20% increase of the initial H_2 production is observed.

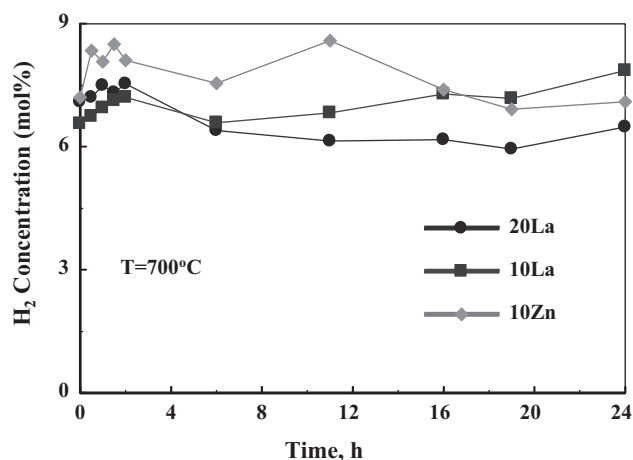
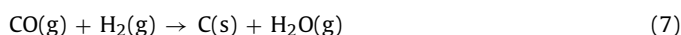
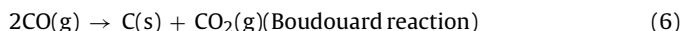


Fig. 12. Stability tests performed on the 0.1 wt% Rh/Mg-Ce-Zr-X-O (X = 10La, 10Zn and 20La) catalysts at 700 °C. Feed gas composition: 0.5% C₆H₅OH/40% H₂O/He; GHSV = 80,000 h⁻¹.

This behavior could be explained as follows. As reaction proceeds, carbonaceous and labile O/OH species accumulate on the support with different rates, where the latter species migrate also towards the Rh metal-support interface. There will be a critical time for an enhanced rate of combustion of the accumulated carbonaceous species due to the establishment of a critical concentration of such oxygen-containing species, which oxidize C_xH_y fragments on the metal, the former originating from phenol decomposition. By comparing the solids containing 10% La and 20% La, it is clearly seen that catalyst stability depends on the La content, in agreement with other studies [92].

Besides the cracking of an oxygenated organic compound that could lead to carbon accumulation on the catalyst surface in steam reforming reactions, as mentioned earlier, other secondary reactions could operate:



Reaction (6) further contributes to the formation of carbonates. In fact, the catalytic performance of these solids coincides very well with what has been reported on the thermal stability of carbonates, where La-carbonates present the highest thermal stability among the rare earth metal carbonates [77]. It is reasonable to expect that by increasing the La content from 10 to 20 at.% more carbonates remain on the surface due to the increased basic character of the surface, which reduces the OSC of support [93]. Moreover, according to Daturi et al. [89], Ce⁴⁺ assists CO₂ incorporation around Zr⁴⁺ cations, leading to higher rates of carbonates formation. According to XPS results to be presented next, 10% La- and 20% La-containing catalysts respond in a different way towards carbonates accumulation/decomposition under H₂ gas treatment. In particular, the 10% La-containing used catalyst (27 at.% Ce³⁺) presented lower carbonates concentration compared to the fresh one. On the other hand, the 20% La-containing catalyst (25 at.% Ce³⁺) presented higher carbonates concentration. It was reported [26] that the formation of carbonates during phenol steam reforming suppresses OSC of similar to the present support compositions.

3.6. X-ray photoelectron spectroscopy studies

Fig. 13 presents Rh 3d XPS spectra obtained on the 0.1 wt% Rh/Mg-Ce-Zr-X-O catalyst (fresh) after calcination at 600 °C in 20% O₂/He for 2 h (**Fig. 13a**), reduced at 300 °C in 20% H₂/He for 2 h (**Fig. 13b**), and after used for 24 h in phenol steam reforming at 655 °C (**Fig. 13c**). For

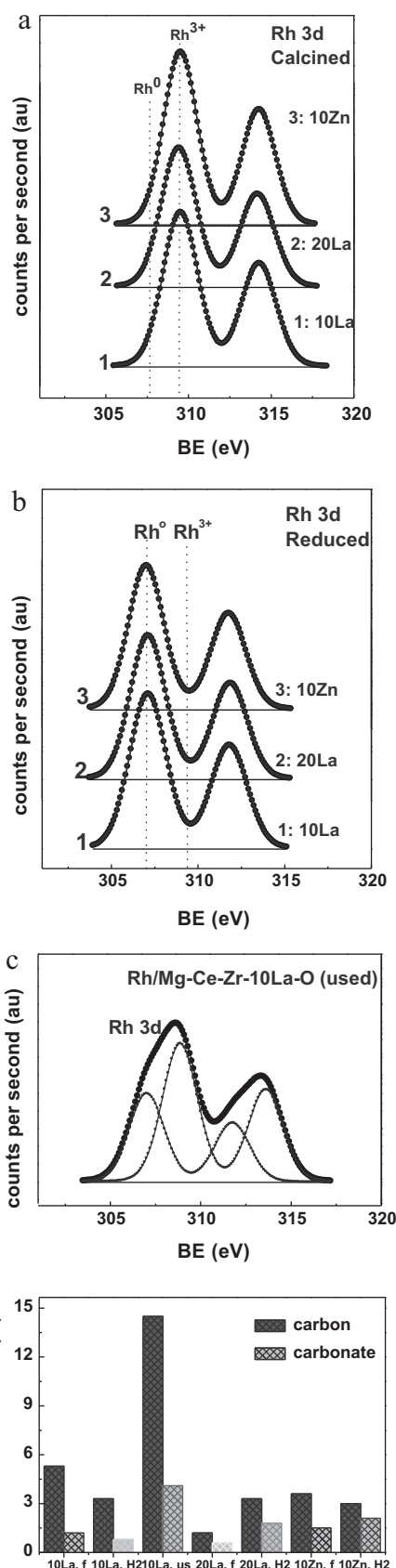


Fig. 13. Rh 3d photoelectron spectra obtained on the 0.1 wt% Rh/Mg-Ce-Zr-X-O catalysts (fresh) after calcination at 600 °C in 20% O₂/He for 2 h (a), reduction at 300 °C in 20% H₂/He for 2 h (b), 24-h phenol steam reforming at 655 °C (c); and (d) “carbon”/carbonates atom percent for the treatments performed in (a)–(c).

Table 4

Binding energies (eV) of core electrons obtained over the 0.1 wt% Rh/Mg-Ce-Zr-X-O (X = La or Zn) catalysts following different gas pretreatments.

Support composition	Zr 3d	Mg 2p	Ce 3d	O 1s	Rh 3d	C 1s	M (La or Zn)
Mg-Ce-Zr-10La-O fresh ^a	182.3	49.6	882.7 (9) ^d	531.3	309.5	284.8 (81) 289.7 (19)	834.8
Mg-Ce-Zr-10La-O H ₂ ^b	182.2	49.6	882.5 (27)	531.4	307.1	284.8 (80) 289.7 (20)	834.7
Mg-Ce-Zr-10La-O used ^c	182.2	49.6	882.5 (12)	531.3	307.0 (39) 308.8 (61)	284.8 (78) 289.9 (22)	834.8
Mg-Ce-Zr-20La-O fresh ^a	182.2	49.8	882.8 (4)	531.2	309.4	284.8 (64) 289.8 (36)	834.9
Mg-Ce-Zr-20La-O H ₂ ^b	182.2	49.7	882.6 (25)	531.1	307.1	284.8 (62) 289.8 (38)	834.6
Mg-Ce-Zr-10Zn-O fresh ^a	182.2	49.6	882.9 (3)	531.2	309.5	284.8 (70) 289.8 (30)	1021.8
Mg-Ce-Zr-10Zn-O H ₂ ^b	182.2	49.8	882.6 (24)	531.3	307.0	284.8 (59) 289.7 (41)	1021.8

^a After synthesis the catalyst was calcined in 20% O₂/He at 600 °C for 2 h.^b The fresh catalyst was reduced in 20% H₂/He at 300 °C for 2 h.^c After phenol steam reforming at 655 °C for 24 h.^d Number in parentheses corresponds to Ce³⁺ percentage (Ce³⁺/(Ce³⁺ + Ce⁴⁺) × 100).

pure Rh metal foil, Rh 3d_{5/2} and Rh 3d_{3/2} peaks occur at 307.0 and 311.8 eV, respectively, with 1.6 eV FWHM [94]. The binding energy of the Rh 3d_{5/2} peak at 307.4 eV is attributed to Rh⁰, while that at 309.7 eV (Fig. 13a) to oxidized Rh particles (Rh³⁺) [95]. Binding energies of Zr 3d, Mg 2p, Ce 3d, Rh 3d, O 1s, C 1s, La 3d and Zn 2p, the latter two coded as M, are reported in Table 4 for the 0.1 wt% Rh/Mg-Ce-Zr-X-O (X = La or Zn) catalysts, after calcination (fresh), reduction in H₂, and phenol steam reforming. For the same catalysts and gas treatments, Table 5 reports the atom % surface composition and the atom % of “carbon” formed as carbonates on the catalyst surface after phenol steam reforming.

In our previous work [38] on the steam reforming of phenol over a 0.1 wt% Rh/50Mg-25Ce-25Zr-O catalyst, it was concluded that reduction of Rh at 300 °C was not complete, and this was attributed to an inherent oxidation of Rh⁰ by surface hydroxyl groups of support. Though in the particular support materials (Mg-Ce-Zr-10X-O, where X stands for La, Zn) of Rh it is observed that rhodium is completely reduced in H₂ at 300 °C, complete reduction of Rh could be attributed to support intrinsic features in agreement with the work of Vis [96] who studied the effect of support (alumina, titania) on Rh dispersion. Nagai et al. [97] addressed the fundamental question as “what property of support does the strength of Pt-oxide–support interaction depend”. They reported that the electron density of oxygen in the support controls the sintering behavior of supported Pt particles, and hence Pt particle size, which in turn affect the extent of reduction of metal particles [97].

In the case of 0.1 wt% Rh/50Mg-25Ce-25Zr-O catalyst [38], Ce appeared as Ce⁴⁺ as opposed to the present case (0.1 wt% Rh/Mg-Ce-Zr-X-O), where Ce⁴⁺ is partly reduced to Ce³⁺ (Table 4, values in parentheses in Ce 3d column). Regarding Ce⁴⁺ → Ce³⁺ reduction and Ce³⁺ presence, the following remarks are appropriate:

(a) Ce³⁺ was found even without any hydrogen reduction treatment, thus it can be attributed to an inherent materials' property related to its composition (La, Zn addition) and synthesis procedure applied. Based on the fact the Ce³⁺ presence

is linked to the presence of oxygen vacancies, it can be said that this result is in agreement with other studies, where La³⁺ addition increases oxygen vacant sites [98].

- (b) Under reducing gas atmosphere, Ce³⁺ concentration in all cases was increased but remained in the same range, namely 24–27 at.% (Table 4). It could be speculated that the nature or the percentage of the fourth element does not influence the extent of Ce³⁺ formation, but is more likely the interactions occurred in the nano-scale domain of Ce⁴⁺ cations which lead to its reduction.
- (c) The 24–27 at.% concentration of Ce³⁺ in the catalyst surface prior to the steam reforming reaction dropped to 12 at.% after reforming (Table 4). Considering the fact that Ce³⁺ ions are coupled with oxygen vacant sites, it can be stated that the latter sites are diminished under reaction conditions, and part of Ce³⁺ ions are oxidized by the high concentration of steam in the feed. This view is in harmony with the steam reforming reaction mechanism suggested [73,79], and proved by our group in earlier studies using transient isotopic experiments [50,51], as well as with the WGS reaction mechanistic routes proposed [77,99]. Stubenrauch and Vohs [100] reported on the interaction of CO with Rh supported on CeO₂(1 1 1) surfaces, stoichiometric and partially reduced, using HREELS and TPD techniques. They found that CO dissociation was by far larger on reduced ceria, and it was correlated with the extent of reduction of CeO₂(1 1 1), implying that oxygen vacancies on the support play a predominant role towards CO dissociation.
- (d) Bearing in mind the low Rh metal loading used (0.1 wt%), and the small mean primary crystallite sizes (15–30 nm) of Mg-Ce-Zr-X-O supports achieved via the sol-gel synthesis used compared to Mg-Ce-Zr-O [38], an enhanced rate of H-spillover from Rh to Mg-Ce-Zr-X-O could explain the facile H₂ reduction of the latter solid.
- (e) The used catalyst presented an increased concentration of Ce³⁺ ions compared to the fresh one, result which implies an assisted reduction of Ce⁴⁺ in the support by the product gases (e.g., H₂ and CO).

Table 5

Atom % surface composition of 0.1 wt% Rh/Mg-Ce-Zr-X-O (X = La or Zn) catalysts estimated by XPS after following different gas treatments.

Support composition	Zr	Mg	Ce	O	Rh	C	La or Zn
Mg-Ce-Zr-10La-O fresh ^a	0.5	27.3	0.2	65.4	0.03	5.3 (1.2) ^d	0.1
Mg-Ce-Zr-10La-O H ₂ ^b	0.5	33.8	0.3	62.3	0.03	3.3 (0.8)	0.1
Mg-Ce-Zr-10La-O used ^c	1.2	37.5	0.6	42.0	0.07	14.5 (4.1)	0.1
Mg-Ce-Zr-20La-O fresh ^a	1.3	34.8	0.5	61.3	0.03	1.2 (0.6)	0.3
Mg-Ce-Zr-20La-O H ₂ ^b	0.7	38.7	0.3	55.0	0.04	3.3 (1.8)	0.2
Mg-Ce-Zr-10Zn-O fresh ^a	1.7	22.1	0.7	69.4	0.04	3.6 (1.5)	0.9
Mg-Ce-Zr-10Zn-O H ₂ ^b	1.6	28.6	0.7	62.9	0.03	3.0 (2.1)	1.1

^a After synthesis the catalyst was calcined in 20% O₂/He at 600 °C for 2 h.^b The fresh catalyst was reduced in 20% H₂/He at 300 °C for 2 h.^c After phenol steam reforming at 655 °C for 24 h.^d Values in parentheses correspond to atom % carbon as carbonates.

According to the results shown in Table 5 and Fig. 13d, the atom % composition of “carbon” and “carbonates” formed after phenol steam reforming compared to the fresh or reduced Rh/Mg-Ce-Zr-10La-O catalysts increases significantly, while at the same time the atom % “oxygen” composition decreases significantly. The increased surface composition of Rh in the used catalyst compared to that in the fresh catalyst is rather related to the significant decrease of oxygen seen by the XPS, due to “carbon” deposition than to a large increase of Rh dispersion during phenol steam reforming.

4. Conclusions

The following conclusions can be derived from the results of the present work:

- The beneficial role of Mg-Ce-Zr-O support used in phenol steam reforming on supported Rh catalyst has been enhanced by adding, via the sol–gel technique, a fourth component from the group of alkaline-earth, rare earth or transition metals.
- By adding an alkaline-earth, rare earth or a transition metal on the Mg-Ce-Zr-O support, the concentration and bonding strength of reducible oxygen species can be tailored.
- The thermal stability of support phases was studied by *in situ* XRD in reductive and oxidative gas atmospheres. FWHM analysis for mean crystalline size estimation was focused on MgO, $\text{Ce}_x\text{Zr}_{1-x}\text{O}_2$ and $\text{LaO}_x(\text{CO}_3)_y$ phases. It was found that the crystallite size of these phases increases under H_2 and decreases under O_2 gas atmospheres.
- Carbonates formation probed by *in situ* XRD and XPS studies does occur under phenol steam reforming reaction conditions.
- XPS studies showed that 0.1 wt% Rh/Mg-Ce-Zr-X-O (X = La, Sr, Ca, Ba, Zn) is largely differentiated from the 0.1 wt% Rh/Mg-Ce-Zr-O in two important aspects. Treatment in H_2 at 300 °C is sufficient for complete reduction of Rh^{3+} into Rh^0 , and Ce^{3+} is present in the 0.1 wt% Rh/Mg-Ce-Zr-X-O catalysts, implying an inherent concentration of oxygen vacant sites in these materials.
- TEM studies showed that MgO formed is spread alone or on top of other support phases, whereas *in situ* XRD studies confirmed its thermal stability.
- The support chemical composition was found to significantly influence the catalytic activity and CO/CO_2 gas product ratio obtained over the Rh/Mg-Ce-Zr-X-O catalysts in the 575–730 °C range for the steam reforming of phenol reaction.
- Acid and basic sites on the surface of Mg-Ce-Zr-X-O support play a major role on the catalytic performance of supported Rh, and also on its coke resistivity through enhancement of carbon gasification rate. Catalysts with the largest concentration of basic sites (10% La- and 20% La-containing) exhibit the best H_2 yields (%).
- Steam was found to remove the accumulated “carbon” species formed during phenol steam reforming at 655 °C or 755 °C in a more efficient way than oxygen. The temperature of reaction seems to regulate the H-deficiency of “carbon” deposited on the catalytic surface; more than one kind of “carbon” species was found to accumulate on the 0.1 wt% Rh/50Mg-25Ce-25Zr-O catalyst. The H/C atom ratio in the accumulated “carbon” depends on the support chemical composition.

Acknowledgements

We acknowledge the financial support by the European Union (ENK5-CT-2001-00545 project, 5th FP), the Cyprus Research Promotion Foundation (TEXNO/MATERIALS/0308(BE)/05), and the Research Committee of the University of Cyprus. The authors are

also thankful to Prof. José-Luis G. Fierro (ICP-CSIC, Madrid, Spain) for the X-ray photoelectron spectroscopy studies.

References

- [1] M.P. Aznar, J. Corella, J. Delgado, J. Lahoz, Ind. Eng. Chem. Res. 32 (1993) 1.
- [2] L. Garcia, M.L. Salvador, J. Arauzo, R. Bilbao, Energy Fuels 13 (1999) 851.
- [3] A. Ishihara, E.W. Qian, I.N. Finahari, I.P. Sutrisna, T. Kabe, Fuel 84 (2005) 1462.
- [4] D. Wang, S. Czernik, D. Montane, M. Mann, E. Chornet, Ind. Eng. Chem. Res. 36 (1997) 1507.
- [5] D. Wang, S. Czernik, E. Chornet, Energy Fuels 12 (1998) 19.
- [6] S. Zinoviev, F. Müller-Langer, P. Das, N. Bertero, P. Fornasiero, M. Kaltschmitt, G. Centi, S. Miertus, ChemSusChem 3 (2010) 1106.
- [7] (a) R.A. Sedjo, Ambio 21 (1992) 274; (b) M.D. Cunningham, J.D. Bishop, H.V. McKay, R.B. Sage, Arbore Monitoring – Ecology of Short Rotation Coppice, DTI Publication URN 04/961, 2004.
- [8] M.K. Mann, P.L. Spath, Life Cycle Assessment of a Biomass Gasification Combined-Cycle System, NREL/TP-430-23076, National Renewable Energy Laboratory (Golden, CO), 1997.
- [9] P.L. Spath, M.K. Mann, Life Cycle Assessment of Coal-fired Power Production, NREL/TP-570-25119, National Renewable Energy Laboratory (Golden, CO), 1999.
- [10] P. Kolbitsch, C. Pfeifer, H. Hofbauer, Fuel 87 (2008) 701.
- [11] K. Aasberg-Petersen, J.-H. Bak Hansen, T.S. Christensen, I. Dybkjaer, P.S. Christensen, C.S. Nielsen, S.E.L.W. Madsen, J.R. Rostrup-Nielsen, Appl. Catal. A: Gen. 221 (2001) 379.
- [12] T.A. Milne, R.J. Evans, N. Abatzoglou, Biomass gasifier Tars: Their Nature, Formation, and Conversion, NREL/TP-570-25357, National Renewable Energy Laboratory (Golden, CO), 1998.
- [13] C. Li, K. Suzuki, Renewable Sustain. Energy Rev. 13 (2009) 594.
- [14] D. Sutton, B. Kelleher, J.R.H. Ross, Fuel Proc. Technol. 73 (2001) 155.
- [15] L. Garcia, R. French, S. Czernik, E. Chornet, Appl. Catal. A: Gen. 201 (2000) 225.
- [16] J. Barbero, M.A. Pena, J.M. Campos-Martin, J.L.G. Fierro, P.L. Arias, Catal. Lett. 87 (2003) 211.
- [17] Z.L. Zhang, X.E. Verykios, Catal. Today 21 (1994) 589.
- [18] O. Yamazaki, T. Nozaki, K. Omata, K. Fujimoto, Chem. Lett. 21 (10) (1992) 1953.
- [19] (a) T. Montini, L. De Rogatis, V. Gombac, P. Fornasiero, M. Graziani, Appl. Catal. B: Environ. 71 (2007) 125; (b) Z. Hou, P. Chen, H. Fang, X. Zheng, T. Yashima, Int. J. Hydrogen Energy 31 (2006) 555.
- [20] K.C. Mondal, V.R. Choudhary, U.A. Joshi, Appl. Catal. A: Gen. 316 (2007) 47.
- [21] H. Jeong, K. Kimb, D. Kimb, I.K. Songa, J. Mol. Catal. A 246 (2006) 43.
- [22] L. Xiancai, W. Min, L. Zhihua, H. Fei, Appl. Catal. A: Gen. 290 (2005) 81.
- [23] T. Horiuchi, K. Sakuma, T. Fukui, Y. Kubo, T. Osaki, T. Mori, Appl. Catal. A: Gen. 144 (1996) 111.
- [24] T. Borowiecki, A. Mochocki, J. Ryczkowski, in: C.H. Bartholomew, J.B. Butt (Eds.), Catalyst Deactivation, Elsevier, Amsterdam, 1994, p. 537.
- [25] T. Borowiecki, Appl. Catal. 10 (1984) 273.
- [26] D.A. Constantinou, A.M. Efstathiou, Appl. Catal. B: Environ. 96 (2010) 276.
- [27] R. Martinez, E. Romero, L. Garcia, R. Bilbao, Fuel. Proc. Technol. 85 (2003) 201.
- [28] D.N. Bangala, N. Abatzoglou, E. Chornet, AIChE J. 44 (1998) 927.
- [29] V.A. Tsipouriari, Z. Zhang, X.E. Verykios, J. Catal. 179 (1998) 283.
- [30] B. Matas Güell, I.V. Babich, L. Lefferts, K. Seshan, Appl. Catal. B: Environ. 106 (2011) 280.
- [31] A. Iriando, V.L. Barrio, J.F. Cambra, P.L. Arias, M.B. Güemez, R.M. Navarro, M.C. Sanchez-Sanchez, J.L.G. Fierro, Catal. Commun. 10 (2009) 1275.
- [32] A.V. Silva Neto, P.P.C. Sartoratto, M.C. Rangel, Stud. Surf. Sci. Catal. 167 (2007) 475.
- [33] J.T. Richardson, B. Turk, M.V. Twigg, Appl. Catal. A: Gen. 148 (1996) 97.
- [34] E. Ruckenstein, Y.H. Hu, Appl. Catal. A: Gen. 133 (1995) 149.
- [35] J.R. Rostrup-Nielsen, in: J.R. Anderson, M. Boudart (Eds.), Catalysis Science and Technology, vol. 5, Springer Verlag, Berlin, 1984, p. 118.
- [36] J.R. Rostrup-Nielsen, in: J.R. Anderson, M. Boudart (Eds.), Catalysis Science and Technology, vol. 5, Springer Verlag, Berlin, 1984, pp. 1–117.
- [37] K. Polychronopoulou, A. Bakandritsos, V. Tzitzios, J.L.G. Fierro, A.M. Efstathiou, J. Catal. 241 (2006) 132.
- [38] K. Polychronopoulou, J.L.G. Fierro, A.M. Efstathiou, J. Catal. 228 (2004) 417.
- [39] K. Polychronopoulou, C.N. Costa, A.M. Efstathiou, Appl. Catal. A: Gen. 272 (2004) 37.
- [40] R. Coll, J. Salvadó, X. Farriol, D. Montané, Fuel. Proc. Technol. 74 (2001) 19.
- [41] D. Wang, S. Czernik, D. Montané, M. Mann, E. Chornet, Ind. Eng. Chem. Res. 36 (1997) 1507.
- [42] C.N. Costa, T. Anastasiadou, A.M. Efstathiou, J. Catal. 194 (2000) 250.
- [43] E. Rohart, O. Larcher, S. Deutsch, C. Hedouin, H. Aimin, F. Fajardie, M. Allain, P. Macaudiere, Top. Catal. 30–31 (2004) 417.
- [44] M. O’Connell, M.A. Morris, Catal. Today 59 (2000) 387.
- [45] M. Hrovat, J. Holc, Z. Samardzija, S. Bernik, J. Mater. Sci. Lett. 19 (2000) 233.
- [46] E. Mamontov, R. Brezny, M. Koranne, T. Egami, J. Phys. Chem. B 107 (2003) 13007.
- [47] T. Montini, A. Speghini, L. De Rogatis, B. Lorenz, M. Bettinelli, M. Graziani, P. Fornasiero, J. Am. Chem. Soc. 131 (2009) 13155.
- [48] G. Balducci, J. Kašpar, P. Fornasiero, M. Graziani, M. Saiful Islam, J. Phys. Chem. B 102 (1998) 557.
- [49] A.D. Mayernick, M.J. Janik, J. Phys. Chem. C 112 (1998) 14955.
- [50] K. Polychronopoulou, A.M. Efstathiou, Catal. Today 116 (2006) 341.

- [51] K. Polychronopoulou, C.N. Costa, A.M. Efstathiou, *Catal. Today* 112 (2006) 89.
- [52] M.A. Johnson, E.V. Stefanovich, T.N. Truong, *J. Phys. Chem. B* 103 (1999) 3391.
- [53] D.B. Williams, C.B. Carter, *Transmission Electron Microscopy: A Textbook for Materials Science*, Springer Verlag, 2009.
- [54] G. Vlaic, R. Di Monte, P. Fornasiero, E. Fonda, J. Kašpar, M. Graziani, *J. Catal.* 182 (1999) 378.
- [55] J.M. Gatica, R.T. Baker, P. Fornasiero, S. Bernal, G. Blanco, J. Kašpar, *J. Phys. Chem. B* 104 (2000) 4667.
- [56] E. Rocchini, M. Vicario, J. Llorca, C. de Leitenburg, G. Dolcetti, A. Trovarelli, *J. Catal.* 211 (2002) 407.
- [57] Q. Yu, X. Wu, C. Tang, L. Qi, B. Liu, F. Gao, K. Sun, L. Dong, Y. Chen, *J. Colloid Int. Sci* 354 (2011) 341.
- [58] P. Fornasiero, R.D. Monte, G.R. Rao, J. Kašpar, S. Meriani, A. Trovarelli, M. Graziani, *J. Catal.* 151 (1995) 168.
- [59] Y. Qiu, J. Chen, J. Zhang, *J. Nat. Gas Chem.* 16 (2007) 148.
- [60] E. Woermann, A. Muan, *Mater. Res. Bull.* 5 (1970) 779.
- [61] S.V. Chavan, A.K. Tyagi, *Thermochim. Acta* 390 (2002) 79.
- [62] L. Xue, Z. Lihua, Z. Chao, Z. Ming, G. Maochu, C. Yaoqiang, *J. Rare Earths* 29 (2011) 544.
- [63] P. Vidmar, P. Fornasiero, J. Kašpar, G. Gubitosa, M. Graziani, *J. Catal.* 171 (1997) 160.
- [64] B. Tang, J. Ge, C. Wu, L. Zhuo, J. Niu, Z. Chen, Z. Shi, Y. Dong, *Nanotechnology* 15 (2004) 1273.
- [65] J.W. Niematsverdriet, *Spectroscopy in Catalysis: An Introduction*, Wiley-VCH, 2000.
- [66] F. Zhong, Y. Xiao, X. Weng, K. Wei, G. Cai, Y. Zheng, Q. Zheng, *Catal. Lett.* 133 (2009) 125.
- [67] S. Kleiman, R. Chaim, *Mater. Lett.* 61 (2007) 4489.
- [68] H. Sieger, J. Suffner, H. Hahn, A.R. Raju, G. Miehe, *J. Am. Ceram. Soc.* 89 (2006) 979.
- [69] J. Huheey, E.A. Keiter, R.L. Keiter, *Inorganic Chemistry: Principles of Structure and Reactivity*, 4th ed., Harper Collins College Publishers, New York, 1993.
- [70] K. Sohlberg, S.T. Pantelides, S.J. Pennycook, *J. Am. Chem. Soc.* 123 (2001) 6609.
- [71] S. Liu, G. Xiong, W. Yang, L. Xu, G. Xiong, C. Li, *Catal. Lett.*, doi:10.1023/A:1019006129861.
- [72] Y.S. Malakhov, G.V. Samsonov, *Poroshkovaya Metallurgiya* 12 (1966) 84.
- [73] M. Assafi, D. Duprez, *Bull. Soc. Chim. Fr.* 1 (1988) 106.
- [74] L. Pino, A. Vita, F. Cipiti, M. Lagana, V. Recupero, *Appl. Catal. B: Environ.* 104 (2011) 64.
- [75] P. Kabner, M. Baerns, *Appl. Catal. A: Gen.* 139 (1996) 107.
- [76] A.M. Maitra, *J. Therm. Anal.* 36 (1990) 657.
- [77] C.M. Kalamaras, P. Panagiotopoulou, D.I. Kondarides, A.M. Efstathiou, *J. Catal.* 264 (2009) 117.
- [78] D.C. Grenoble, *J. Catal.* 51 (1978) 212.
- [79] D. Duprez, P. Pereira, A. Miloudi, R. Maurel, *J. Catal.* 75 (1982) 151.
- [80] J.R.H. Ross, M.C.F. Steel, A. Zeini-Isfahani, *J. Catal.* 52 (1978) 280.
- [81] C. Diagne, H. Idriss, A. Kiennemann, *Catal. Commun.* 2 (2002) 565.
- [82] B.M. Weckhuysen, G. Mestl, M.P. Rosynek, T.R. Krawietz, J.F. Haw, J.H. Lunsford, *J. Phys. Chem. B* 102 (1998) 3773.
- [83] H. Remy, *Treatise on Inorganic Chemistry*, vol. 1, Elsevier, Amsterdam, 1996.
- [84] S. Nouisir, S. Keav, J. Barbier Jr., M. Bensitel, R. Brahmi, D. Duprez, *Appl. Catal. B: Environ.* 84 (2008) 723.
- [85] A.G. Dedov, A.S. Loktev, I.I. Moiseev, A. Aboukais, J.-F. Lamonier, I.N. Filimonov, *Appl. Catal. A: Gen.* 245 (2003) 209.
- [86] P. Fornasiero, G. Balducci, R. Di Monte, J. Kašpar, V. Sergo, G. Gubitosa, A. Ferrero, M. Graziani, *J. Catal.* 164 (1996) 173.
- [87] L. Castoldi, R. Matarrese, L. Lietti, P. Forzatti, *Appl. Catal. B: Environ.* 90 (2009) 278.
- [88] W.S. Abdel Halim, A.S. Shalabi, *Solid State Commun.* 124 (2002) 67.
- [89] M. Daturi, C. Binet, J.C. Lavalley, G. Blanchard, *Surf. Interface Anal.* 30 (2000) 273.
- [90] R. Di Monte, J. Kašpar, *J. Mater. Chem.* 15 (2005) 633.
- [91] R.J. Koestner, M.A. van Hove, G.A. Somorjai, *J. Phys. Chem.* 87 (1983) 203.
- [92] S.H. Park, B.-H. Chun, S.H. Kim, *Korean J. Chem. Eng.* 28 (2) (2011) 402.
- [93] (a) S. Nouisir, S. Keav, J. Barbier, M. Bensitel, R. Brahmi, D. Duprez, *Appl. Catal. B: Environ.* 84 (2008) 723;
- (b) X. Wang, R.J. Gorte, *Appl. Catal. A: Gen.* 224 (2002) 209.
- [94] M. Kawai, M. Uda, M. Ichikawa, *J. Phys. Chem.* 89 (1985) 1654.
- [95] T. Lopez, A. Lopez-Gaona, R. Gomez, *Langmuir* 6 (1990) 1343.
- [96] J.C. Vis, *J. Mol. Catal.* 25 (1984) 367.
- [97] Y. Nagai, T. Hirabayashi, K. Dohmae, N. Takagi, T. Minami, H. Shinjoh, S. Matsumoto, *J. Catal.* 242 (2006) 103.
- [98] T.K. Bhattacharya, A. Ghosh, H.S. Tripathi, S.K. Das, *Bull. Mater. Sci.* 26 (2003) 703.
- [99] C.M. Kalamaras, S. Americanou, A.M. Efstathiou, *J. Catal.* 279 (2011) 287 (and references therein).
- [100] J. Stubenrauch, J.M. Vohs, *Catal. Lett.* 47 (1997) 21.